Bioactive ECM-mimicking nerve guidance conduit for enhancing peripheral nerve repair

Shuang Liu [a,1], Julia Simińska-Stanny [b,1], Lizhao Yan [c,1], Lihong Fan [a,**], Xiaoyue Ding [d],
Tengda Ma [a], Wei Guo [d], Yingsong Zhao [e], Ming Li [a], Jianghai Chen [e],
Oseweuba Valentine Okoro [b], Armin Shavandi [b], Lei Nie [b,d,*]

[a] *School of Chemistry, Chemical Engineering and Life Sciences, Wuhan University of Technology, Wuhan, 430070, China*
[b] *Université Libre de Bruxelles (ULB), École Polytechnique de Bruxelles, 3BIO-BioMatter, Avenue F.D. Roosevelt, 50 - CP 165/61, 1050, Brussels, Belgium*
[c] *Department of Hand Surgery, Union Hospital, Tongji Medical College, Huazhong University of Science and Technology, Wuhan, 430022, China*
[d] *College of Life Sciences, Xinyang Normal University, Xinyang, 464000, China*
[e] *Department of Emergency Surgery, Union Hospital, Tongji Medical College, Huazhong University of Science and Technology, Wuhan, 430022, China*

ARTICLE INFO

ABSTRACT

Extensive research efforts are being directed towards identifying alternatives to autografts for the treatment of peripheral nerve injuries (PNIs) with engineered nerve conduits (NGCs) identified as having potential for PNI patients. These NGCs, however, may not fulfill the necessary criteria for a successful transplant, such as sufficient mechanical structural support and functionalization. To address the aforementioned limitations of NGCs, the present investigation explored the development of double cross-linked hydrogels (o-CSMA-E) that integrate the biocompatibility of porcine tendon extracellular matrix (ECM) with the antimicrobial and conductive properties of methacrylated quaternary chitosan. The hydrogels had matrices that could promote the growth of axons and the transmission of neural signals. The hydrogels were subsequently incorporated into a nanofibrous PLLA-ZnO sheath scaffold (ZnO@PLLA) to emulate the natural nerve structure, guiding cell growth and facilitating nerve regeneration. The collaboration of core and sheath materials in ZnO@PLLA/o-CSMA-E nerve guidance conduits resulted in enhanced migration of Schwann cells, formation of myelin sheaths, and improved locomotion performance in rats with sciatic nerve defects when *in vivo* studies were undertaken. Notably, the *in vivo* studies demonstrated the similarity between the newly developed engineered NGCs and autologous transplants, with the newly engineered NGCs possessing the potential to promote functional recovery by mimicking the tubular structure and ECM of nerves.

1. Introduction

Despite the recent advancements in tissue engineering, autografts or autologous nerve grafting has remained the benchmark for restoring neural transmittance following peripheral nerve injury (PNI) [1]. Size mismatching and limited availability of autografts present unfavorable circumstances for patients and impose a significant burden on clinical practice [2,3]. Providing stable structural support until a sufficient regeneration of the nerve is achieved constitutes a major challenge in nerve regeneration. In PNIs, artificial nerve conduits typically implemented as alternatives to autologous nerve grafting [4,5]. Nerve guidance conduits (NGCs) are tubular biostructures engineered to provide a supportive microenvironment while also guiding axonal growth across the nerve injury site [2]. Various biological and artificial NGCs, utilizing biomaterials from natural and synthetic polymers, have been developed for peripheral nerve regeneration to optimize the microenvironment and mimic the natural regeneration process [6–8]. Current fabrication techniques for NGCs primarily involve injection molding, melt extrusion, and film rolling to replicate the tube-like structure of nerves [9–11]. Other approaches, including coaxial biofabrication and extrusion bioprinting, which are gaining increasing attention, also fall short when it comes to porous structures [12,13]. Crucially, however,

---

acknowledging the impact of morphological structure on cellular regeneration, the techniques of electrospinning and melt-electro writing have emerged as promising approaches for generating microporous sheaths in NGCs [9]. Indeed, the potential for electrical transmittance in electrospinning biomaterials was demonstrated in the work of Javidi

and Xu. They showed that electrospinning fibers doped with ZnO exhibited highly efficient transduction of piezoelectric signals [14,15]. Similarly, electrospinning polycaprolactone-PCL/ZnO or PLLA/ZnO fibers have also been used to create porous NGC sheaths with inherent structural and electrical stimulation properties that promote axonal
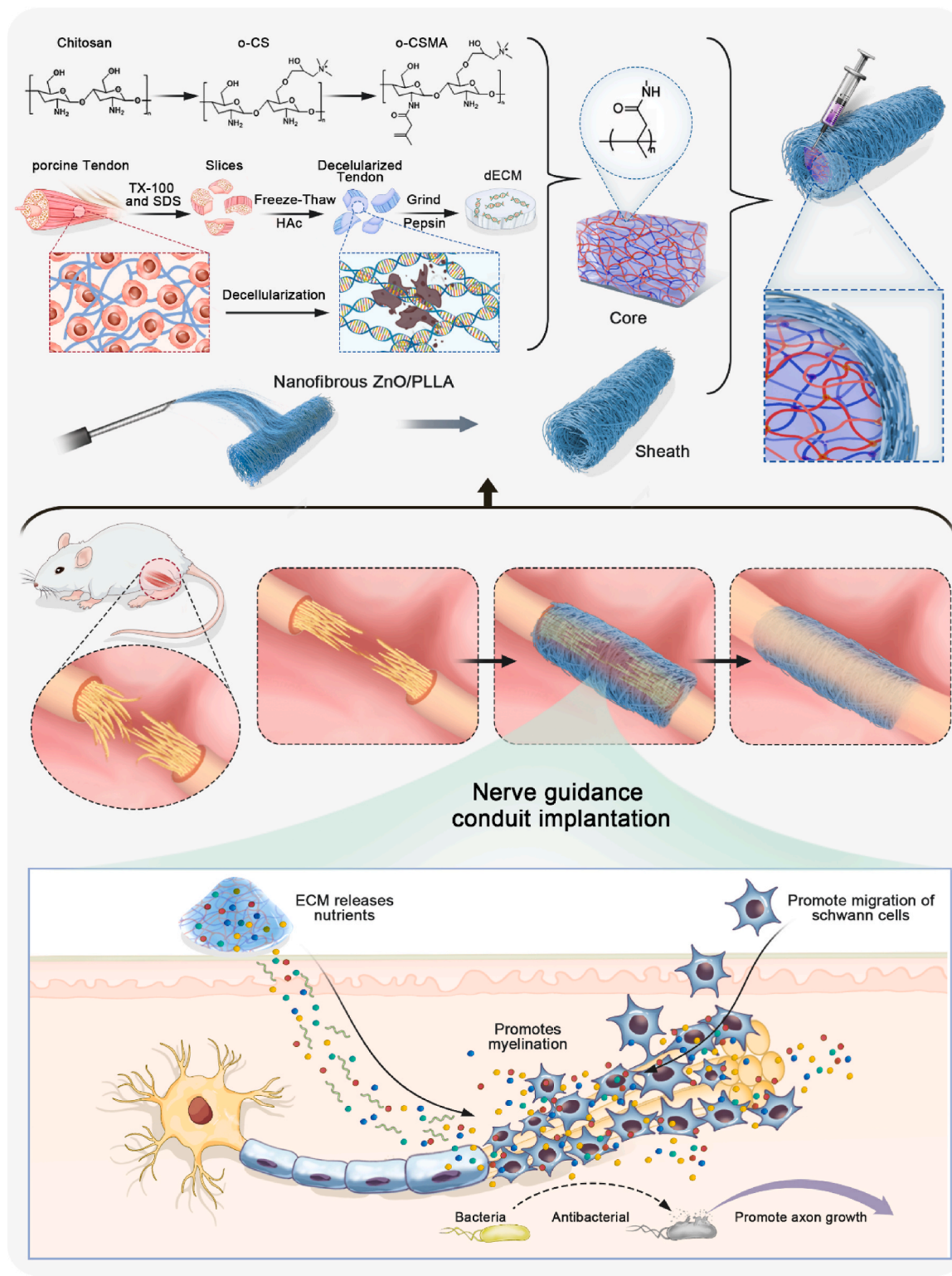
Scheme 1. Schematic illustration showing fabrication of nerve conduits (NGCs) using core and sheath structures. The electrospinning nanofibrous ZnO@PLLA scaffold serves as the sheath, and methacrylated quaternary chitosan crosslinked with dECM as the core. The fabricated NGCs for treating peripheral nerve injury (PNI) have the potential to facilitate peripheral nerve regeneration and functional recovery.

regeneration [14,16]. Nevertheless, as mature neurons have a low regenerative capacity, hollow NGCs do not fulfil the requirements for effective nerve restoration [2,3].

Hollow NGCs lack internal architecture, potentially causing misdirection of regenerating axons due to the axons' inability to navigate effectively [2,6]. Hence, through the incorporation of topological cues from porous conductive nanofibers and biochemical cues derived from natural-based hydrogel fillings [17] within a dual core-sheath structure [18], a novel category of composite conductive material for nerve regeneration has been developed. Natural and especially decellularized extracellular matrix (dECM)-derived hydrogels have a beneficial influence on tissue regeneration due to their tunable viscoelasticities [2,19, 20], their ability to trigger the release of bioactive molecules, and growth factors, and activate stem cells towards new tissue formation [21,22]. Poly (L-lactide) (PLLA) electrospinning fibers decorated with dECM hydrogel were reported to improve sciatic nerve function regeneration when compared with plain PLLA fibers [23]. The application of hydrogels based on dECM in nerve conduit development can expand the sources for potential nerve conduit materials, providing a high structural mimicry to the native counterparts [1]. Electrical conductivity is another factor pointed to be crucial in NGCs-core-filling materials for the regulation of cell metabolism, adhesion, proliferation, migration, and differentiation [24–26]. Scientists explored conductive polymers such as polyaniline (PANI), PEDOT: PSS [27], and quaternary ammonium salts of natural polymers [28–30].

With these contexts in mind, the present study proposes the integration of piezoelectric zinc oxide (ZnO) from electrospinning PLLA fibers with quaternary chitosan salt in a dECM-hydrogel-based nerve sheath filler to fabricate a novel nerve conduit with regenerative potential. The quaternary ammonium groups on the chitosan backbone rendered the material conductive and highly antimicrobial [31–33], while dECM provided biological cues such as sites for cell adhesion [34] or proper viscoelasticity [19] to mimic the native environment of axonal growth and myelination. The inclusion of the ZnO powder improved cell migration, re-epithelialization, and angiogenesis, which is crucial for healing and regeneration [35].

This is the first report utilizing quaternary salt of chitosan-dECM with electrospinning ZnO@PLLA chitosan for the fabrication of a nerve conduit (Scheme 1). The utilized ZnO@PLLA sheath with tuned nanofibers resulted in a permeable nerve graft, which navigated Schwann cell migration and myelin sheath formation, promoted the restoration of damaged nerve connections.

2. Experimental section

2.1. Materials

Chitosan (deacetylation degree 80–95 % and viscosity of 200–800 cP), glycidyl trimethyl ammonium chloride (GMTAC, 95 %), N-hydroxysuccinimide (NHS), 1-ethy-3-(3-dimethylaminopropyl carbodiimide) hydrochloride (EDC), and Poly-L-lactic acid (PLLA) (Mw = 100 000) were purchased from Sigma-Aldrich Co., Ltd. Phosphate buffer salt (PBS), nano zinc oxide (ZnO), dopamine (DA), benzaldehyde, ethyl alcohol, isopropanol, acetone, methylene dichloride (DCM), sodium carbonate, and methacrylic anhydride ($C_8H_{10}O_3$) were purchased from Aladdin Co., Ltd. Samples of porcine tendon were obtained from Wuchang Slaughterhouse (Wuhan, China). Photoinitiator LAP2959 was purchased from McLean. Sodium hydroxide (NaOH), acetic acid (CH_3COOH, HAc), and hydrochloric acid (HCl) were purchased from Sinopharm Chemical Reagents Co., Ltd. All reagents were purchased and used directly without further purification. Millipore water was prepared using a Milli-Q50 SP Reagent Water System (Millipore Corporation, USA).

2.2. Synthesis of methacrylated quaternary salt of chitosan (o-CSMA)

2.2.1. Synthesis of quaternary chitosan salt (o-HACC)

The quaternary chitosan salt (o-HACC) was prepared following a method described in the literature [36]. Specifically, 2.0 g chitosan powder was added to 90 mL of deionized water. After stirring and dispersing, 10 mL of acetic acid solution was added and stirred at room temperature until dissolved. The mixture was stored at 4 °C for 12 h until completely swollen, and then 80 mL of anhydrous ethanol was added to the solution. Next, 10 g of benzaldehyde solution was added to 20 mL of ethanol and slowly poured into a separating funnel to the stirred chitosan solution at room temperature. Once the dripping was completed, the temperature of the solution was increased to 60 °C and high-speed stirring continued for 10 h. Then, 50 mL of anhydrous ethanol was added to cool down and terminate the reaction. A 100 mL of sodium hydroxide solution (1 mol/L) was added to the solution, producing a large amount of white flocculent precipitates. After filtration, the product was washed with anhydrous ethanol three times and dried at 50 °C for 24 h to obtain N-benzylidene chitosan.

The dried product was ground into powder using a mortar and added to 20 mL of 40 % sodium hydroxide solution. The solution was stirred at 60 °C for 2 h, filtered and vacuum dried to obtain alkaline N-benzylidene chitosan. The dried powder was added to 120 mL of isopropanol solution, stirred at room temperature for 2 h, and heated up to 70 °C. Then 8.0 g of 3-epoxypropyltrimethylammonium chloride was added and stirred at high speed for 24–30 h. The reaction was then cooled to room temperature and precipitated with 30–50 mL of acetone. After filtration, it was washed with anhydrous ethanol. The reaction product was vacuum dried at 50 °C for 24 h to obtain N-benzylidene chitosan grafted with quaternary ammonium salt. The vacuum-dried powder was added to a 200 mL hydrochloric acid ethanol solution with a concentration of 0.25 mol/L and stirred at room temperature for 24 h. The pH was adjusted to neutral with a 1 % sodium carbonate aqueous solution, then precipitated with acetone again, filtered and dried to obtain the crude product. The crude product was dialyzed for 3 days and finally lyophilized to obtain o-chitosan quaternary ammonium salt (o-HACC).

2.2.2. Synthesis of methacrylated quaternary salt of chitosan (o-CSMA)

O-chitosan quaternary salt (o-HACC) was further modified with acryloyl groups to obtain methacrylated quaternary salt of chitosan (o-CSMA). In this regard, o-HACC was dissolved in PBS solution (10 w/v%) and reacted with methacrylic anhydride (8 h at 50 °C). Then, the reaction solution was stopped using PBS (around 5 times the react solution volume). Next, the resulting mixture was dialyzed (12–14 kDa) in distilled water for 7 days at room temperature. The final o-CSMA was obtained after freeze-drying.

2.3. Preparation and analysis of decellularized ECM using porcine tendon tissue

2.3.1. Preparation of decellularized ECM

The decellularized extracellular matrix (dECM) was prepared using methods described in the literature [21]. Briefly, porcine tendons were cut into fine pieces and washed in PBS for 2 h. Next, the tendon tissues were immersed in 0.5 % SDS and 0.5 % Triton X-100 for 24 h, followed by washing with PBS. Next, 1 v/v% HAc solution was added for 24 h and then washed for 48 h with distilled water. Tendons, after the series of treatments, were freeze-dried and milled. Powdered dECM was frozen and stored.

2.3.2. Composition and functional analysis of decellularized ECM

SDT buffer (4 % SDS, 100 mM Tris-HCl, pH 7.6) was added to dECM and transferred to 2 mL quartz sand tubes. After that, the mixture was homogenized using an MP Fastprep-24 automated homogenizer (6 M/s, 30 s, twice), and the obtained homogenate was sonicated and boiled for 10 min. Next, the sample was centrifuged (14 000 g) for 15 min, and the

supernatant was filtered using a 0.22 μm filter. The filtered sample was quantified using the BCA Protein Assay Kit (P0012, Beyotime). Next, the sample was treated using FASP digestion. Briefly, 50–200 μg of proteins were reduced using DTT (100 mM) for 5 min at 100 °C. Then, DTT, detergent and other low-molecular-weight components were removed using UA buffer (8 M Urea and 150 mM Tris-HCl, pH 8.5) with ultra-filtration (Sartorius, 30 kD) three times. After that, 100 μL iodoaceta-mide (100 mA IAA in UA buffer) was added to the block-reduced cysteine residues, and the samples were incubated shielding from light for 30 min. The filters were washed using NH_4HCO_3 buffer (50 mM) twice and UA buffer three times. Then, the protein suspensions were digested using trypsin (Promega) overnight at 37 °C, and the collected peptides were desalted using the C18 column. Mass spectrometry (LC-MS/MS) was performed using an Orbitrap Exploris 480 spectrometer (Thermo Fisher Scientific). Data was searched against the Uniprot database (Uniprotkb_Sus scrofa (pig)_333 488_20 240 102_9823) employing the label-free quantification approach (data-dependent acquisition, and data-independent acquisition) using MaxQuant soft-ware (version 1.6.17.0). For the bioinformatics analysis, gene ontology (GO) and Kyoto encyclopedia of genes and genomes (KEGG) pathways were employed to analysis the obtained dECM.

In addition, in vivo biocompatibility assessements of the dECM were undertaken. All animal procedures were performed in this work following the guidelines of the "Principles of Laboratory Animal Care" (NIH publication No. 8523, revised in 1985), and the experimental protocol was approved by the Animal Ethics Committee of Tongji Medical College, Huazhong University of Science and Technology (Approval Number 3726). The six-week old Sprague Dawley rats were anaesthetized using 50 mg/kg of 2 % pentobarbital, the dECM was implanted into the subcutaneous place, and 2 weeks later, the tissue was collected for quantitative immunofluorescence staining (CD3, α-SMA, iNOS, and ARG1).

2.4. Preparation of o-CSMA-E hydrogels

To obtain hydrogel materials with varying content of dECM, a 5 wt% solution of acrylic acid-modified quaternary ammonium chitosan (o-CSMA) was prepared. o-CSMA solution was mixed with a certain quantity of dECM at 37 °C for 16 h. When the mixture attained homo-geneity, 400 μL of photoinitiator solution (5 wt%) was added and mixed for 30 s. To obtain stable hydrogels the as-prepared precursor solutions were photocured for 5 min with 360 nm ultraviolet light. The final product was dialyzed in distilled water for 24 h and freeze-dried for 48 h to obtain the core hydrogel for NGC preparation. The composite hydrogel sample is named o-CSMA-E x, where *x* represents the mass ratio of dECM to o-CSMA polymer.

2.5. Preparation of NGCs

To prepare electrospinning NGC sheaths, a 10 wt% solution of PLLA/DCM was prepared and dopped with a certain mass of nano-ZnO powder (Table S1, Supplementary Materials). The Polymeric mixture was mixed evenly and used for electrospinning (Shenzhen Tongli Micro-Nano Technology Co., Ltd.; TL-OMNI-BM). A 22G needle with a flow rate of 0.8 mL/h, and a voltage of ±12 kV was used. The rotating mandrel collector was placed within 10 cm from the outlet of the needle and set to rotate at 300 rpm. When the electrospinning was complete, the NDC was removed from the collector, resulting in a fibrous ZnO@PLLA tube. A ZnO@PLLA sheath was loaded with a lyophilized o-CSMA-E hydrogel to obtain composite NGC. The as-prepared conduit was left to swell in PBS and later used for subsequent tests and animal experiments.

2.6. Characterization methods

2.6.1. ^1H Nuclear magnetic resonance (^1H NMR) analysis
The materials (chitosan, o-HACC, o-CSMA) were dissolved in D_2O,

and subsequently transferred into the nuclear magnetic tubes. The nu-clear magnetic resonance spectra were recorded using JEOL ECZ600R/S3spectrometer (^1H NMR, 600 MHz) [36].

2.6.2. Fourier-transform infrared spectroscopy (FT-IR) analysis
The structure and presence of specific chemical groups in chitosan, o-HACC, and o-CSMA were confirmed by Fourier-transform infrared spectroscopy (FT-IR, PerkinElmer Spectrum 2) [37]. The FT-IR spectra were obtained within a resolution of 1 cm^{-1} between 500 and 4000 cm^{-1}.

2.6.3. UV–Vis spectroscopy
The diffuse reflectance spectra of ZnO@PLLA with different amounts of ZnO were investigated using Ultraviolet–visible Spectroscopy (UV–Vis, PerkinElmer, Lambda 950) with equipping an integrating sphere attachment. The prepared polymeric blends were operated in the range of 200–500 nm at 298 K [38].

2.6.4. X-ray diffractometer (XRD) analysis
An X-ray powder diffractometer (XRD, Rigaku Smartlab 9 kW) was used to obtain XRD patterns of o-CSMA-E hydrogels and ZnO@PLLA polymeric blends. A spinning sample holder was used, and settings were adjusted as follows: 45 kV and 200 mA with Cu Kα radiation ($\lambda = 1.5406$ Å). Data were acquired in the 2θ range of 5~90° with a 10° step increment.

2.6.5. Scanning electron microscope (SEM) analysis
To observe the pore size and morphology of hydrogels and electro-spinning PLLA blends used to prepare the core and sheath of NGC a scanning electron microscope (SEM, Hitachi Regulus8220) was used. Prior to the observations, hydrogels were freeze-dried. Samples were sprayed with a platinum layer, before imaging.

2.6.6. Hydrophilicity test via water contact angle analysis
The hydrophilicity test was carried out using a water contact angle meter (OCA4, Dataphysics, Germany). 5 μL deionized water was drop-ped on the electrostatically spun catheter material, and the contact angle was recorded at the 5th second from the beginning of the droplet's contact with the nanofibers. The average value was obtained from a minimum of three independent measurements.

2.6.7. Mechanical properties evaluation
The mechanical properties of NGCs must be evaluated to ensure their suitability for nerve repair and regeneration. Cyclic compression and release testing with 20 % maximum compressive strain and 1 mm/min compression rate were conducted [39].

2.6.8. Piezoelectric measurement
Piezoelectric voltage signals were detected from ZnO@PLLA fibers using a simple impulse loading test setup. A sample (1 × 1 cm) was placed between two sheets, and different weights fell down on the sample from a fixed height (1 cm). Next, the generated voltage was detected via assembled devices of pre-amplifier and high impedance mixed domain oscilloscope [40].

2.6.9. Rheological properties analysis
The rheological performance of o-CSMA-E hydrogels was evaluated by a TA rheometer (DHR-2, USA) with 1 % constant strain and a constant frequency of 10 rad/s at 37 °C. Time, temperature and frequency sweep tests were performed for hydrogels (o-CSMA-E 0.05, o-CSMA-E 0.1, o-CSMA-E 0.2.) A low inertia parallel plate (40 mm) setup with a 1 mm gap was used to perform measurements. To avoid evaporation of the sample's water the edges were sealed using glycerin.

2.6.10. Water absorption and degradation
The freeze-dried o-CSMA-E hydrogels were first weighted and sub-

sequently immersed in distilled water for 24 h to reach saturation. Then, the swollen hydrogel was gently dried with tissue paper, and the sample mass was recorded. The water absorption rate was calculated (Eq. (1)).

$$WAR = \frac{m_2 - m_1}{m_1} \times 100\% \qquad \text{(Eq. 1)}$$

where WAR, m_1 and m_2 denote the water absorption rate (dimensionless), the initial mass of the freeze-dried o-CSMA-E hydrogels in g, and the mass of the swollen hydrogels in g.

2.6.11. Degradation

To investigate the degradation behavior of o-CSMA-E hydrogels and ZnO@PLLA polymeric blends, dried samples were immersed in simulated body fluid (SBF) for 24 h to reach swelling equilibrium. The mass was recorded initially as (m_0). Next, the swollen samples were immersed in SBF, sealed, and placed in a shaking incubator at 37 °C (100 rpm/min). The samples were taken out at the predesignated time, and their masses were recorded (m). The degradation rate (DD) was then calculated (Eq. (2)).

$$DD = \left(1 - \frac{m_0 - m_1}{m_0}\right) \times 100\% \qquad \text{(Eq. 2)}$$

where m_0 and m_1 denote the initial mass of the o-CSMA-E hydrogels and ZnO@PLLA polymeric blends in g and the mass of the swollen o-CSMA-E hydrogels and ZnO@PLLA polymeric blends in g.

2.6.12. Antibacterial activity evaluation

The antibacterial response of hydrogel materials against Gram-negative *E. coli* (ATCC 25922) and Gram-positive *S. aureus* (ATCC 6538) was determined following the same procedures as in our previous publication [41].

2.6.13. Cell culture

The Murine pheochromocytoma (PC12) neuronal cells supplied by Shanghai Zhong Qiao Xin Zhou Biotechnology Co (Shanghai, China) were cultured in RPMI 1640 medium (Gibco., USA) supplemented with 10 % fetal bovine serum and 1 % streptomycin penicillin. Cells were cultured at 37 °C with a 5 % CO_2 humidified atmosphere, and the medium was changed every two days. When the cell density reached 80 %, cells were detached using trypsin and re-suspended in a new cell medium. Cells from passage three were used for the experiments.

2.6.14. Biocompatibility and cell proliferation evaluation

Confluent PC12 cells were detached using 0.25 % trypsin EDTA and seeded onto the NGCs with a density of approximately 1×10^4 cells/well. Prior to the experiments, NGCs were sterilized by soaking in 75 % ethanol for 2 h, washed three times with PBS, and then exposed to UV light for 4 h. Cell Counting Kit 8 (CCK 8, Beyotime Biotechnology) was used to estimate cell proliferation and viability after 24, 48, 72 h after seeding. Briefly, CCK 8 reagent was added to each well and incubated at 37 °C for 2 h, next absorbance at 450 nm was measured using a microplate reader (Varioskan ™ LUX, Thermo Fisher Scientific), and the relative viability was calculated in relation to the control [26]. Live-/Dead Assay kit (Beyotime Biotechnology) was used on day 3 and day 7 to reassess viability. Cells were stained with Calcein AM (green) and propidium iodide (red) according to the manufacturer's instructions. After staining, cells were observed under a fluorescence microscope, and micrographs were randomly taken during fluorescence inspection.

2.6.15. Cell migration assay–scratch assay analysis

To evaluate the impact of NGCs on PC12 cells migration, a wound area was created by culture inserts (Ibidi GmbH, Martinsried, Germany). After which 70 μL of PC12 cell suspension at a density of 4×10^5 cells/mL was added into two wells. The cells were then incubated in a complete medium for 24 h then the inserts were removed, resulting in the

formation of a 500 μm cell-free gap. The gap closure was monitored for 24 h in the presence of NGCs. Images of cells were captured using an inverted microscope at different times (0, 8, 24 h). ImageJ software (https://doi.org/10.1038/nmeth.2089) was used to estimate the relative healing rate of the wound area.

2.6.16. In vivo model establishment

Adult male Sprague Dawley rats (weight 250 g) were used for the experiments and all animal procedures followed the "Principles of Laboratory Animal Care" (NIH publication No. 8523, revised in 1985), and the approved experimental protocol (Approval Number 3726). The animals were anaesthetized with 50 mg/kg of pentobarbital (2 %). The surgical site was shaved and disinfected using iodine and alcohol. From the posterior, access the right sciatic nerve was exposed. The proximal 5 mm of the nerve was transected, and a 10 mm segment was removed, followed by bridging the gap with 15 mm sterile NGC. The NGCs were sutured to the epineurium of the nerve stumps, and the muscle and skin incisions were closed. After surgery, the rats were placed on a warm pad to recover from anaesthesia and returned to their cages.

2.6.17. Walking trajectory analysis

A walking trajectory analysis was used to evaluate the severed nerves. The hind paws of the rats were marked with red dye, with the right paw set as the experimental group and the left as the control. A narrow dark box lined with white paper with a light source at the end was prepared and used to collect rats' footprints when passing the corridor. Each footprint was subjected to measurements, such as the distance from the heel to the tip of the third toe (PL), the spread from the first to the fifth toe (TS), and the spread between the second and fourth toes (IT). The procedure was repeated three times for each animal, and average values were used in calculations. Next, a Sciatic Function Index (SFI) was calculated (Eq. (3)) to quantify the functional recovery progress [1,26].

$$SFI = -38.3 \frac{EPL - NPL}{NPL} + 109.5 \frac{ETS - NTS}{NTS} + 13.3 \frac{EIT - NIT}{NIT} - 8.8$$
$$\text{(Eq. 3)}$$

where 'E' represents the measurements related to the experimental group and 'N' for control.

2.6.18. Gastrocnemius muscles wet weight determination and histological evaluation

The gastrocnemius muscles from operated and contralateral normal limbs were compared and weighed after 8 weeks of implantation. The wet weight ratios of the operated side to the healthy side were calculated [42]. For further histological evaluation, the gastrocnemius muscles were fixed, embedded, and sectioned for HE staining and Masson's trichrome staining treatment. HE and Masson staining images were obtained by a light microscope. Next, the muscle fiber and collagen fiber were quantitively evaluated using ImageJ software based on six random staining images [39].

2.6.19. Electrophysiological evaluation of regenerated sciatic Nerve

Electrophysiological evaluations were carried out to monitor the functional recovery of nerves, 8 weeks post-surgery in comparison to uninjured nerves. Electrical stimuli (pulse signal with intensity of 0.7 mA, duration of 5 ms, and filtered between 1-10 Hz and 10–1000 Hz) were sequentially applied to the proximal and distal ends of the graft site. Recording electrodes on the triceps muscles allows the recording of the compound muscle action potentials (CMAPs). Peak-to-peak amplitude measurements were performed from the most positive to the most negative deflection [26]. For each NGC group, the percentage of the CMAP amplitude (% CMAP) was calculated (Eq. (4)).

$$\% \, CMAP = \frac{CMAP \, amplitude \, of \, NGC \, group}{CMAP \, amplitude \, of \, uninjured \, nerves} \times 100\% \qquad \text{(Eq. 4)}$$

The time delay between the electrical stimulus and the onset of the resultant CMAP was used to determine motor nerve conduction velocity (MNCV) – Eq. (5).

$$MNCV = \frac{Distance\ between\ electrodes\ [cm]}{Time\ delay\ [ms]} \qquad (Eq.\ 5)$$

All measurements were performed using the BL420 system Taimeng, Chengdu, China, ensuring that data acquisition parameters remained consistent within experiments.

2.6.20. Western blot analysis

The quantitative profiling of neurofilament 200 (NF200) and myelin basic protein (MBP) in regenerated neural tissues was conducted via Western Blotting techniques. Tissue specimens were washed with phosphate-buffered saline and homogenized in RIPA lysis buffer supplemented with protease inhibitors, followed by centrifugation to extract the protein lysates. Protein concentrations were ascertained employing the bicinchoninic acid (BCA) assay. The proteins were segregated by SDS-PAGE and electrophoretically transferred to polyvinylidene difluoride (PVDF) membranes pre-activated with methanol. Immunodetection involved the use of primary antibodies specific to NF200 sourced from ProteinTech (catalog #18934-1-AP, China) and to MBP from Affinity Biosciences (catalog #AF4085, China), with subsequent application of horseradish peroxidase (HRP)-conjugated secondary antibodies. Bands were detected using an enhanced chemiluminescence (ECL) system, and densitometry was performed with a gel documentation system to quantitatively analyze the expression levels of the proteins under study [26].

2.6.21. Transmission electron microscopy (TEM) evaluation

After 4 weeks post-surgery, the regenerated nerves from rats (randomly selected) for each group were collected, and transmission electron microscopy (TEM) images were used for the analysis of myelin sheath thickness, G-ratio, and myelinated axon number. After a series of fixations, dehydration, embedding, and ultrathin sectioning, the obtained sections were stained for TEM observation. In addition, Image J software was used for further quantitative analysis of the myelin sheath's quantity, G-ratio and thickness.

2.6.22. Histological evaluation

To evaluate nerve regeneration and anastomosis at 4 and 8 weeks after implantation surgery, the rats were euthanized, and the regenerated nerves were carefully harvested. After overnight fixation in 4 % paraformaldehyde and dehydration in graded ethanol, tissues were embedded in paraffin and sectioned longitudinally into 5 μm thick slices. Following standard protocols, the sections were stained with hematoxylin-eosin (HE) and Masson's trichrome staining. For HE staining, paraffin was removed, and samples were rehydrated. The staining solution was applied for 5 min, washed in running tap water, differentiated in 1 % acid alcohol (30 s), and washed again. After that, counterstaining in eosin phloxine solution was performed (1 min) and dehydrated through graded ethanol. For Masson's trichrome staining, sections were mordanted in preheated Bouin's solution at 56 °C for 15 min. After rinsing in running tap water, the sections were stained with Weigert's iron hematoxylin (10 min), followed by washing and rinsing. Then, Biebrich scarlet acid fuchsin staining solution was applied (5 min), washed first in distilled water, and then differentiated in phosphomolybdic phosphotungstic acid solution for 10–15 min. After rinsing, sections were transferred into an aniline blue solution and stained for 5–10 min. Finally, after HE and Masson's trichrome staining were completed, stained sections were cleared in xylene, covered with mounting medium and observed under a light microscope for histological analysis.

2.6.23. Immunofluorescence staining

To evaluate the nerve regeneration, immunofluorescence staining of S100 (red) was carried out to observe Schwann cells, and NF 200 (green) staining was used to observe axons. Myelin basic protein (MBP, green) and β tubulin (red) staining were performed to simultaneously visualize myelin sheaths and axons. Briefly, the nerve sections were deparaffinized, rehydrated, and subjected to antigen retrieval. Samples were blocked with 5 % bovine serum albumin (BSA), and incubated with primary antibodies: mouse anti-S100 (1:200), rabbit anti-NF 200 (1:400), mouse anti-MBP (1:500) and rabbit anti β tubulin (1:200), overnight at 4 °C. This step was followed by incubation with fluorescently labelled secondary antibodies for 1 h at room temperature. The nuclei were counterstained with DAPI for 5 min. Finally, images were taken with a fluorescent microscope.

2.7. Statistical analysis

Each experiment was repeated three times unless stated otherwise. Values were presented as the mean ± standard error. Mean values were compared using one-way analysis of variance (ANOVA) with SPSS.22 statistical software package, and pairwise comparison was carried out with the Bonferroni method with statistical significance established when $p < 0.05$, unless stated otherwise.

3. Results and discussion

3.1. Obtaining dECM

According to our previous work, dECM was obtained by decellularizing the porcine Achilles tendon tissue [39,43]. The synthesized dECM treated using a series of SDS, Triton X-100, and HAc, displayed good water absorption performance, excellent cytocompatibility, abundant type I collagen, and effective decellularization, proving potential for peripheral nerve regeneration. Gene ontology (GO) term enrichment and Kyoto Encyclopedia of Genes and Genomes (KEGG) pathway analysis were used to further understand the composition and function of dECM. Crucially dECM, participates in various biological processes, eg. metabolic, developmental, immune and stimulus-response actions. Additionally, it may facilitate binding and catalyzing functions (Fig. 1A and B). All cellular regions, namely cytoplasm, extracellular space, nucleus, mitochondria and cell membrane, contain ECM. Traces of ECM may also be found in the endoplasmic reticulum, peroxisome and cytoskeleton (Fig. 1C). The molecular weight of ECM's proteins is mainly 10–80 kDa, and the length of the peptide 8–30 amino acids (Fig. 1D–F).

The biocompatibility of isolated dECM was investigated in a rat model. Compared with the control group (no dECM), there was no difference in the expression of CD3, while aSMA was slightly reduced. In the dECM treated group, expression of macrophage-specific markers (iNOS and ARG1) was significantly decreased (Fig. 1G and H). These results indicated that the obtained dECM has good biocompatibility, with potential for the biomedical field.

3.2. Preparation and properties of core part of NGC

In this study, the naturally derived dECM and chemically modified chitosan were combined to create a favorable environment for axonal regeneration [44]. Fig. 2A shows that the chitosan was first grafted with benzaldehyde, after which conjugation with 2,3-epoxypropyl trimethyl to give o-quaternaryl-N-benzylidene chitosan (OB-HACC). OB-HACC subsequently reacted with HCl, resulting in the formation of o-chitosan quaternary salt (o-HACC). Quaternary ammonium groups grafted onto the chitosan backbone increase its conductivity [45], making the synthesized material a potential candidate to support nerve regeneration. The synthesis route was validated by NMR and FT-IR spectra. The FT-IR signals (Fig. 2B) revealed a band of the quaternary salt positioned at 1488 cm^{-1}, resulting from asymmetric angular bending of methyl groups of quaternary hydrogen in o-HACC [29,30]. The N–H bending (1600 cm^{-1}) of the primary amine was weakened in chitosan salt as the
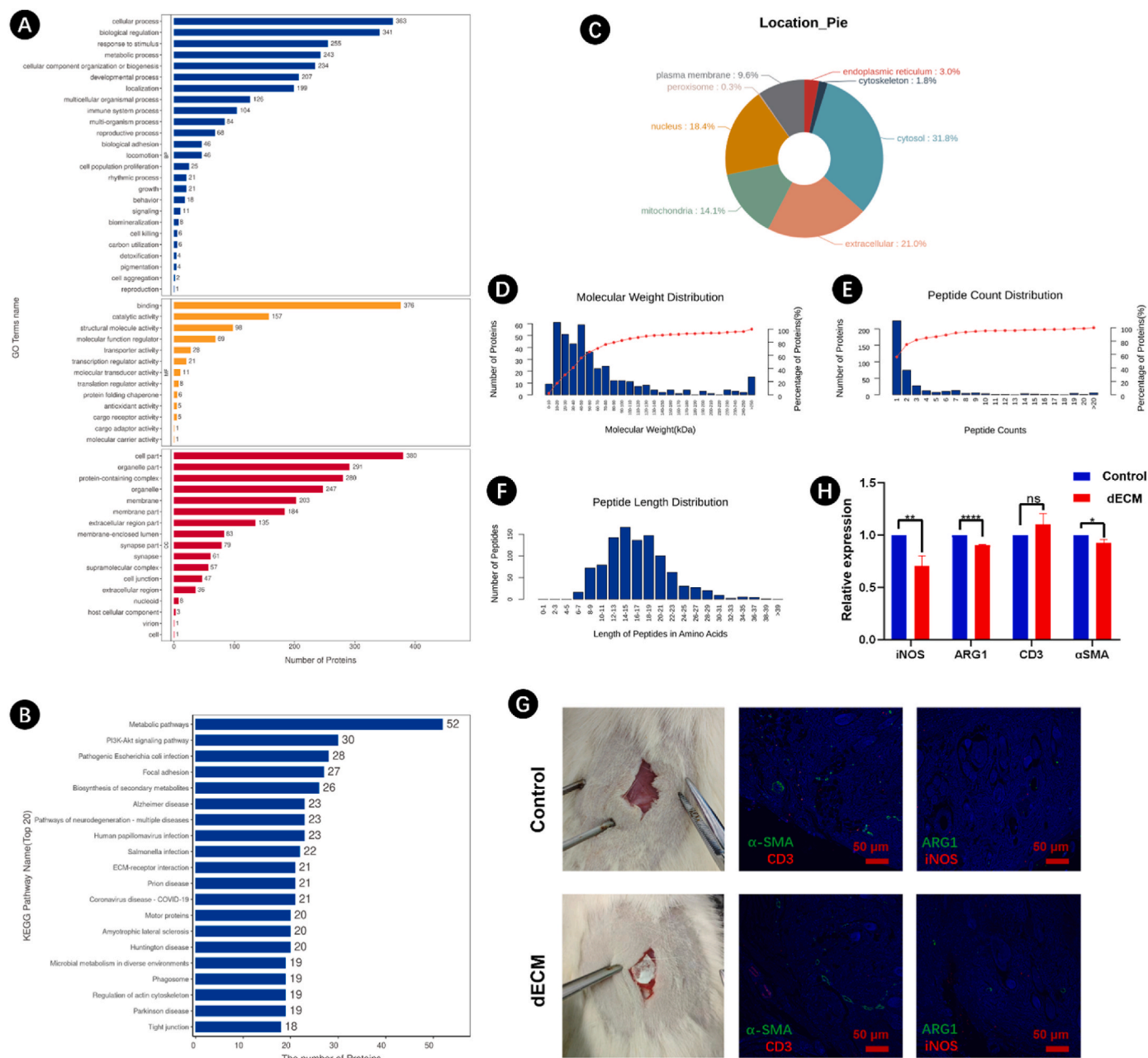
Fig. 1. (A) Gene ontology (GO) term enrichment analysis, (B) Kyoto Encyclopedia of Genes and Genomes (KEGG) pathway analysis, and (C) subcellular localization of decellularized ECM (dECM) using porcine Achilles tendon. (D) Molecular weight distribution of proteins, (E) peptide count distribution, and (F) peptide length distribution in obtained dECM. (G) *In vivo* evaluation of dECM using SD rats, the obtained dECM was implanted in subcutaneous tissue, and immunofluorescence staining (α-SMA, CD3, ARG1, and iNOS) at 6 weeks post-surgery, the scale bar: 50 μm. (H) Quantification analysis of the stained areas.

primary amine shifted to the secondary aliphatic amine [29,30,46]. Moreover, the peak at 3.2 ppm in the ¹H NMR spectrum of o-HACC confirmed the presence of three methyl groups [30] (Fig. 2C). The obtained quaternary salt of chitosan (o-HACC) was further modified with acryloyl groups (MA), enabling compound photopolymerization. Fig. 2B shows that compared to o-HACC, the peak ascribed to the symmetrical bending vibration of -CH_3 of the quaternary ammonium group (1488 cm^{-1}) in o-CSMA is less prominent [47]. Additionally, the o-CSMA spectra also show bands at 1650 cm^{-1} and 1540 cm^{-1} corresponding to amide (I) and amide (II), respectively, and is indicative of the incomplete deacetylation of N-acetyl-d-glucosamine units [47,48]. The NMR spectra presented in Fig. 2C show that the o-CSMA spectra presented new resonance signals at shifts 5.65 ppm and 5.25 ppm corresponding to methylene and methacrylamide, respectively, indicating that the

o-HACC was methacrylated [48,49].

Fig. 3A shows that functional, conductive hydrogels were obtained after mixing acrylic acid-modified quaternary ammonium chitosan (o-CSMA) solution (5 wt%) with LAP2959 photoinitiator. Despite being conductive, hydrogels comprising single-crosslinked networks often suffer from poor mechanical properties, low bioactivity, and enhanced or delayed degradation, which seriously affects their practical application, especially in the field of regenerative medicine [28]. The strategy of incorporating dECM can boost the biological activity of single-network hydrogels and create an interpenetrating polymeric network (IPN) when crosslinked using EDC/NHS chemistry [21,50]. For this experiment, dECM was obtained from a porcine Achilles tendon, following the treatment process as described previously [21]. o-CSMA hydrogel was mixed with a certain amount of dECM material to form
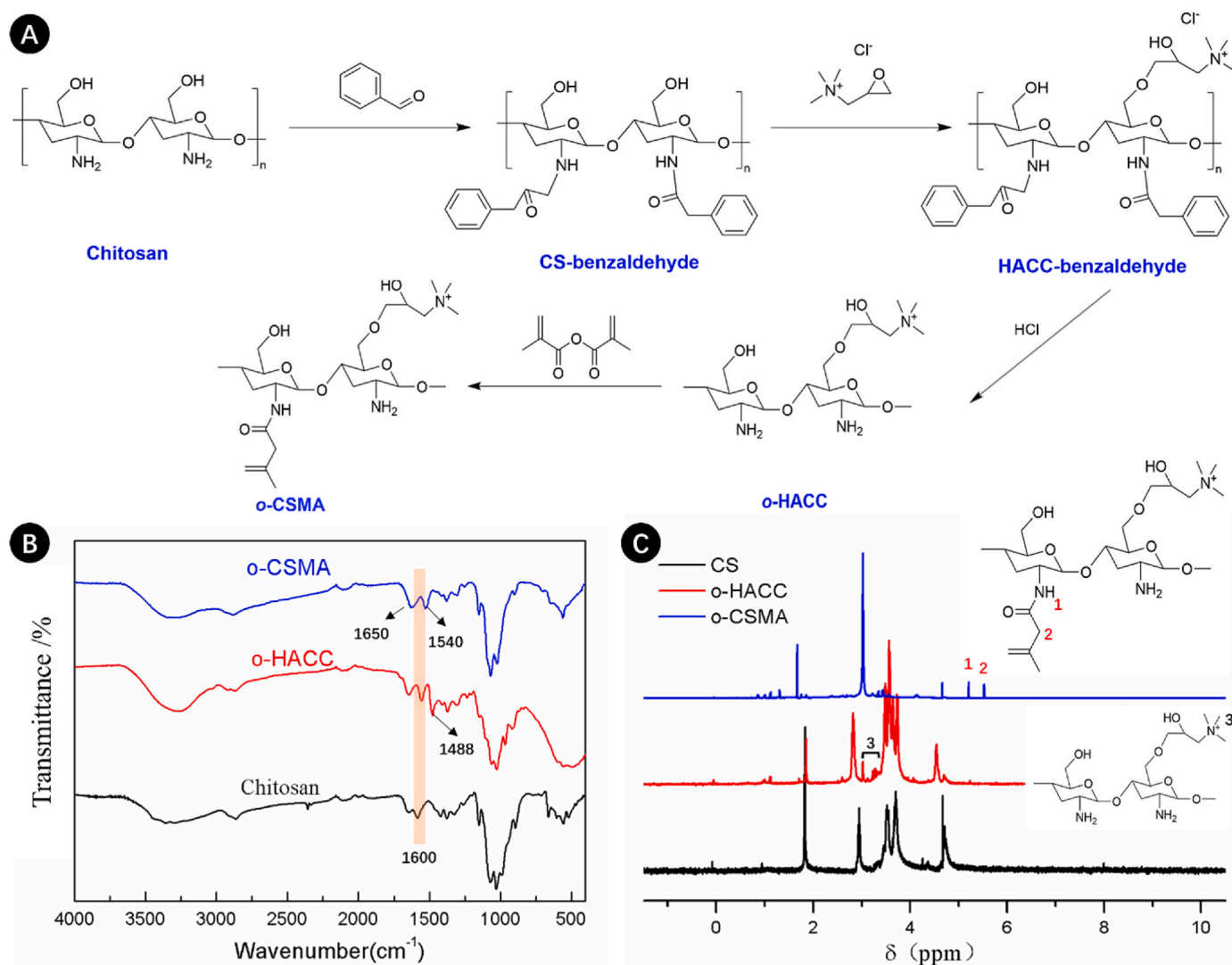
Fig. 2. (A) Route of the synthesis leading to methacrylated quaternary salt of chitosan (o-CSMA); FTIR spectra (B) and ^{1}H NMR spectra (C) of chitosan, quaternary salt of chitosan (o-HACC) and methacrylated quaternary salt of chitosan (o-CSMA).

quaternized chitosan-ECM hydrogels (o-CSMA-E hydrogels). This was followed by photocuring and crosslinking with EDC/NHS [21]. The as-prepared hydrogels could be successfully crosslinked and form a stable structure when the dECM concentration did not exceed 0.4 % (Fig. 3B). It is proposed that O-CSMA-E hydrogels, with a dECM content below 0.4 %, exhibit stability and the ability to replicate the conduction of electrical signals observed in neural tissue. Furthermore, these hydrogels are anticipated to create conditions favorable to appropriate responses from nerve cells to external stimuli [44]. Regardless of the presence of dECM, the hydrogels exhibited a porous structure conducive to facilitating cellular ingrowth (Fig. 3C and Fig. S1, Supplementary Materials). Fig. 3F shows that the o-CSMA hydrogels have larger pores than o-CSMA-E hydrogels, although their pore geometries are similar. It is important to note that imaging dry samples may not accurately reflect the porous properties of the scaffold material, highlighting one of the limitations of our study.

A negative impact of increasing dECM content on pore connectivity was observed and subsequently attributed to structural collapse. Notably, Fig. 3E also shows that by increasing dECM content from 0.05 to 0.2 %, the water absorption capability of the hydrogels increased by 150 %. However, in the case of 0.4 % dECM, hydrogel swelling decreased as the degradation mechanisms accelerated significantly compared with other groups (Fig. 3G). Similarities could be observed in

hydrogels' XRD traces (Fig. 3D). The main peak at approximately 21° and a weak peak at 7°, proved hydrogel crystallinity [41], thus the presence of an organized structure. With respect to the degradation rates, the hydrogels with 0.05–0.4 % dECM degraded within 16–30 days, demonstrating sufficient durability and degradation time required to provide space for the newly formed neural tissue [51].

To withstand internal body forces, hydrogels must show time and temperature stability [52]. Fig. 3H and I shows the rheological properties of the o-CSMA-E hydrogels. The G′ and G″ of hydrogels remained independent of time (Fig. 3H), but in the temperature sweep test (Fig. 3I) hydrogel's G′ decreased gradually with an increase in dECM content, indicating a weakening of the hydrogel's elastic strength. In frequency sweep experiments, the hydrogels showed a comparable pattern of behavior (Fig. 3J), the o-CSMA-E 0.1 hydrogel demonstrated greater strength in the low-frequency region, followed by a transition from elastic to viscous behavior as the frequency increased.

Favorable hydrogel antibacterial activity reduces the risk of possible bacterial infection [41], with chitosan identified as a major natural polymer that is endowed with abundant antimicrobial behavior [30]. Therefore, as expected, all tested hydrogels exhibited antibacterial behavior (Fig. 4). Additional analysis was undertaken to determine the degree of light scattering by bacteria [53] using optical density (OD) measurements at 600 nm with the results presented in Fig. 4A and B. The
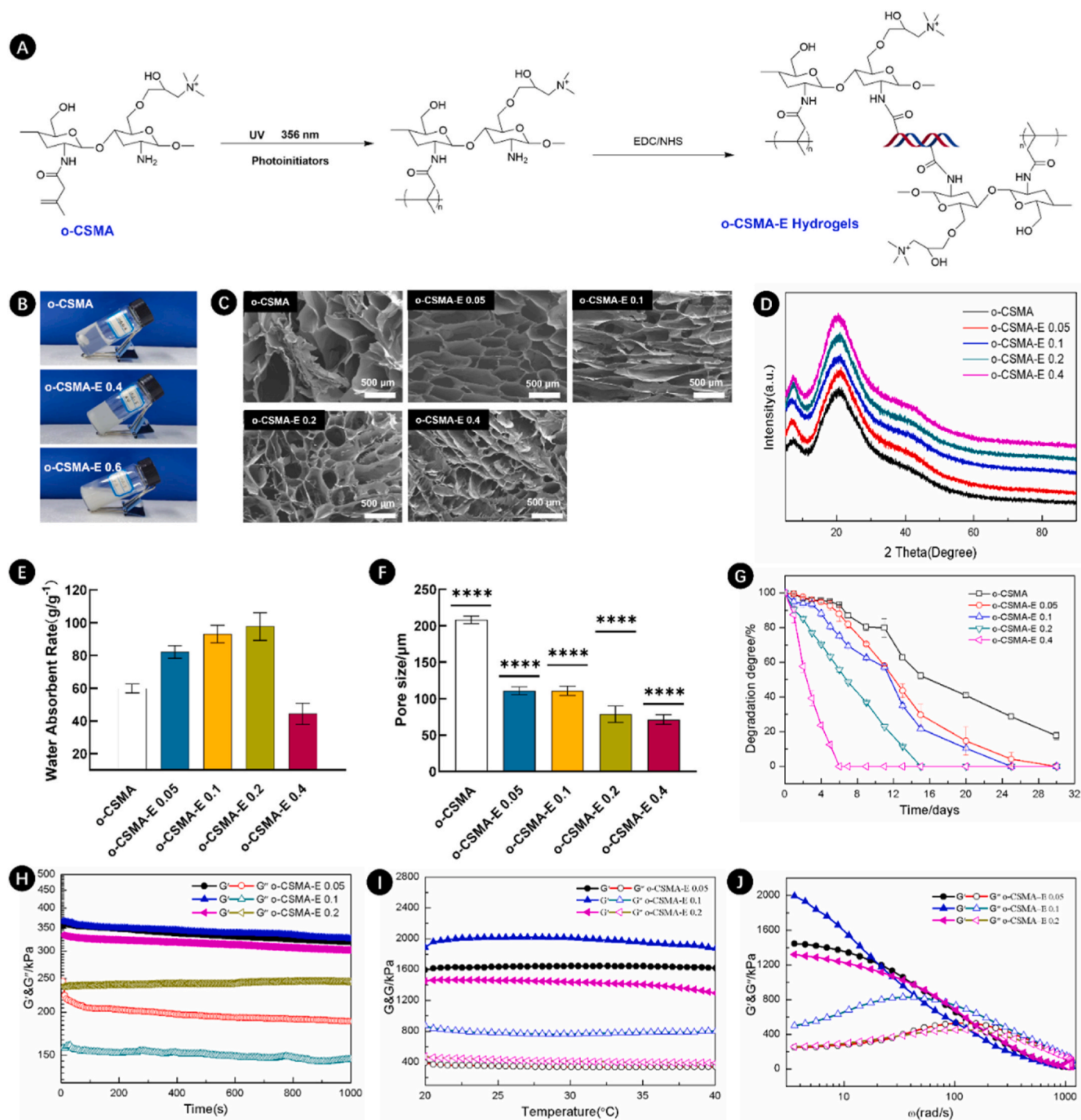
Fig. 3. A) Reaction scheme illustrating the process of o-CSMA-E hydrogels formation; B) Photographic images of formed hydrogels (o-CSMA, o-CSMA-E 0.4, and o-CSMA-E 0.6); C) SEM images showing the microstructure of o-CSMA and o-CSMA-E hydrogels (o-CSMA-E 0.05, o-CSMA-E 0.1, o-CSMA-E 0.2, and o-CSMA-E 0.4); D) XRD characterization of o-CSMA-E hydrogels with different ratio of dECM (0, 0.05, 0.1, 0.2 and 0.4); E) Water absorbent rate, F) pore size distribution, and G) degradation degree of o-CSMA and o-CSMA-E hydrogels; H) time sweep test, I) temperature sweep test, and J) frequency sweep test of o-CSMA-E hydrogels, ****p < 0.0001.

results showed that o-CSMA-E hydrogels were more efficient in resisting bacterial growth, compared to the blank sample. Especially, O-CSMA-E 0.1 and O-CSMA-E 0.2 demonstrated an effective broad-spectrum antibacterial property, as no or few colonies could be detected (Fig. 4C-E and Table S2, Supplementary Materials). An inhibition zone test results presented in Fig. 4F–I were consistent with antibacterial activity results discussed earlier, with all hydrogels shown to demonstrate good antibacterial activity towards both Gramm (+) and (−) bacterial species

[41]. The favorable antibacterial properties of the synthesized hydrogels may be due to the elevated surface charge of the quaternary ammonium salt group ($-NR_3^+$), which facilitates the disruption of the bacterial cell wall [28].

The core of NGCs with extracellular matrix proteins replicating the natural dECM and conductive counterparts for signal transmission can be employed to interact with cells to enhance regeneration [2]. Furthermore, materials for the NGCs should support the chemical,
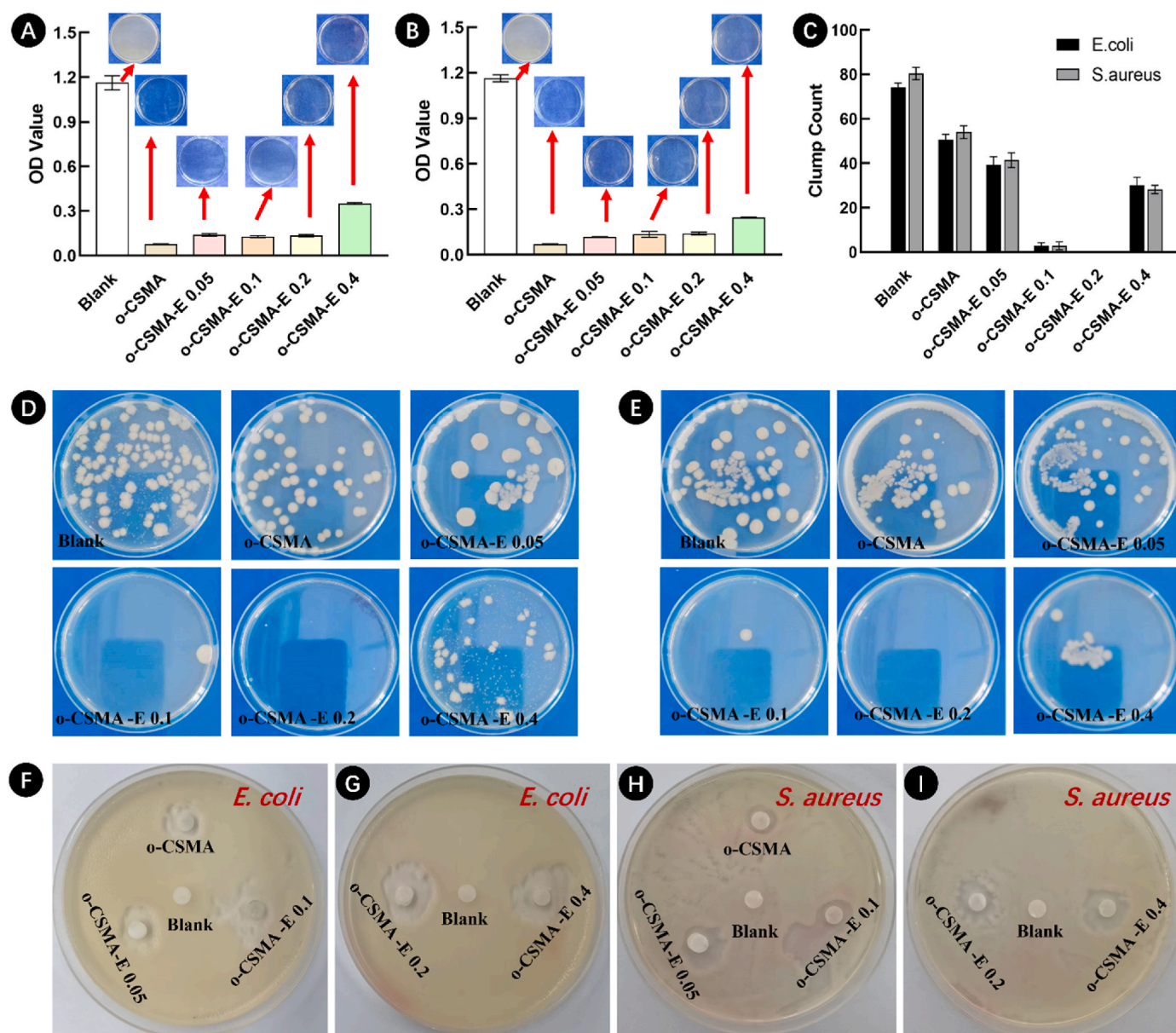
Fig. 4. The antibacterial behavior of O-CSMA and O-CSMA-E hydrogels sterilized 0.9 % saline solution, served as the control group. Optical density (OD) measurements for samples tested against (A) *E. coli* (gram-negative) and (B) *S. aureus* (gram-positive); C) Bacterial colonies count for different hydrogel samples; Photographs of the antibacterial activity of the hydrogels against (D) *E. coli* and (E) *S. aureus* (gram-positive); The inhibitory zone radius of the hydrogels against (F, G) *E. coli* and (H, I) *S. aureus*, sample placed in the middle of the dish served as experiment control.

physical and biological surroundings of neural and glial cells [44]. The O-CSMA-E 0.2 hydrogel was identified as the most suitable candidate, meeting the criteria of adequate stability and antimicrobial activity, and used as the core for the engineered NGCs in subsequent experiments.

3.3. NGCs sheath fabrication and morphological characterization

The electrospinning method was used to fabricate the NGC sheaths. Previous studies have emphasized its superiority over other manufacturing techniques, such as freeze-drying or lyophilization, solvent casting, gas foaming, and 3D printing [6,9,10]. Specifically, electrospinning enables the development of nanofibrous substrates that can mimic ECM with fibers ranging from 50 to 500 nm in diameter [54]. Electrospinning is an efficient method for fabricating nanofiber conduits as it results in a large surface area with a porous, ECM resembling structure [55,56]. The electrospinning method was utilized, and the performance of the PLLA solution was analyzed after doping with zinc

oxide (ZnO). The partial dissolution of ZnO leads to the release of zinc ions (Zn^{2+}), having antimicrobial activity against multiple strains of bacteria and fungi [57,58].

We have carefully adjusted the polymer solution flow rate and the distance between the needle and the collector to perform electrospinning of PLLA solution with different ZnO content (Table S1, Supplementary Materials). Electrospinning was performed on a rotating mandrel, resulting in a nanofibrous sheath for NGCs (Fig. 5A). The tubular architecture of electrospinning material can later ease the implantation procedure by aligning the proximal and distal stump of the injured nerve, providing confined microenvironments for nerve restoration [6].

Fig. 5B shows the resulting electrospun fibers with macroporosities created by deposited fibers and microporosities of the fibers (magnified images in Fig. 5B). Fibrillar porosity may provide contact guidance for regenerating axons [56] and exhibit a well-aligned orientation to direct the axonal cell growth in the appropriate direction [2]. Previous studies
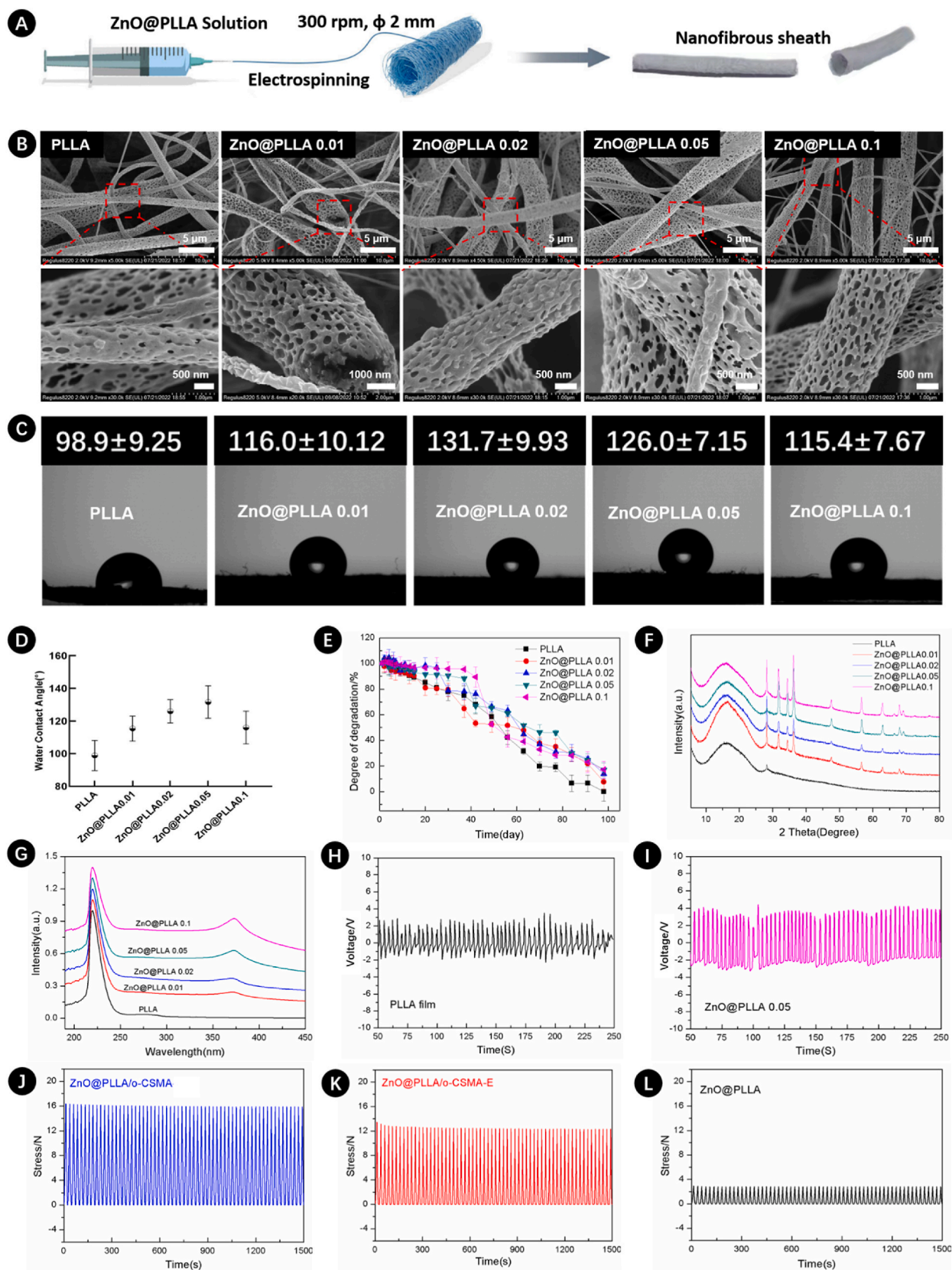
Fig. 5. A) Schematics of the NGCs electrospinning process using a rotating mandrel, with the fabricated NGC on the right side; B) SEM images of nanofibers obtained by electrospinning of PLLA dopped with different ratios of ZnO; C) Photographs demonstrating water contact angles of ZnO@PLLA surfaces with increasing ZnO content from left to right and D) water contact angles graph; E) Assessment of the degradation performance of different ZnO/PLLA conduits; F) XRD spectra and G) UV–Vis spectra of ZnO@PLLA fibers and PLLA. Voltages observed from H) PLLA film and I) Zn@PLLA 0.05 fiber. The cyclic compression behavior of J) ZnO@PLLA/o-CSMA, K) ZnO@PLLA/o-CSMA-E, and L) ZnO@PLLA.

demonstrated that Schwann cells could elongate along fibers if their diameter is around 1~1.3 μm [56,59]. However, diameters that are too large or too small may hamper axonal growth [59]. A positive correlation was observed between the water contact angle of the electrospun fibers and increasing ZnO content thus demonstrating the increasing hydrophobic nature of electrospinning fibers (Fig. 5C). Fig. 5C and **D** also show that when the ZnO content reached 0.1 g, the water contact angle was similar to PLLA with 0.01 g of ZnO in the electrospinning polymeric blend. The degradation kinetics of NGC sheath were also investigated, and the results are presented in Fig. 5E. Fig. 5E shows that all tested materials, regardless of ZnO content, showed similar degradation patterns, and after 100 days, electrospinning scaffolds had no more than 20 % of their initial weight. Structure's ability to gradually degrade in SBF is sufficient to support tissue regeneration and at the same time avoid the need to perform secondary surgery for graft removal. To verify the presence of ZnO in PLLA-based electrospinning solutions and gain information about material crystallinity XRD and UV–Vis experiments were performed (Fig. 5F and **G**). Typical XRD patterns associated with crystal planes of the hexagonal ZnO structure

[60], appeared when PLLA was dopped with ZnO. Similarly, UV–Vis spectra revealed an emission peak at ~370 nm ZnO presence [60], the intensity of XRD and UV–Vis peaks increased with increasing ZnO content. In addition, the voltage detected from PLLA film was in the range of 1.12–3.24 V, and the voltage from ZnO@PLLA 0.05 fiber was in the range of 2.23–4.65 V (Fig. 5H and **I**). The observed voltage from ZnO@PLLA fiber confirms its potential to produce electrical stimulation, which is suitable in nerve regeneration applications. For further verifying NGCs in nerve repair and regeneration, the mechanical properties were performed, and the cyclic compression performance of NGCs was shown in Fig. 5J–L. Sample ZnO@PLLA/o-CSMA displayed the highest stress, and all samples maintained their integrity after 100 cycles of compression.

3.4. NGCs assembly and biocompatibility investigations

Nanofibrous scaffolds lacking internal architecture may not effectively guide axonal growth, potentially resulting in misdirected ingrowth and innervation failure [2,6]. However, the incorporation of a
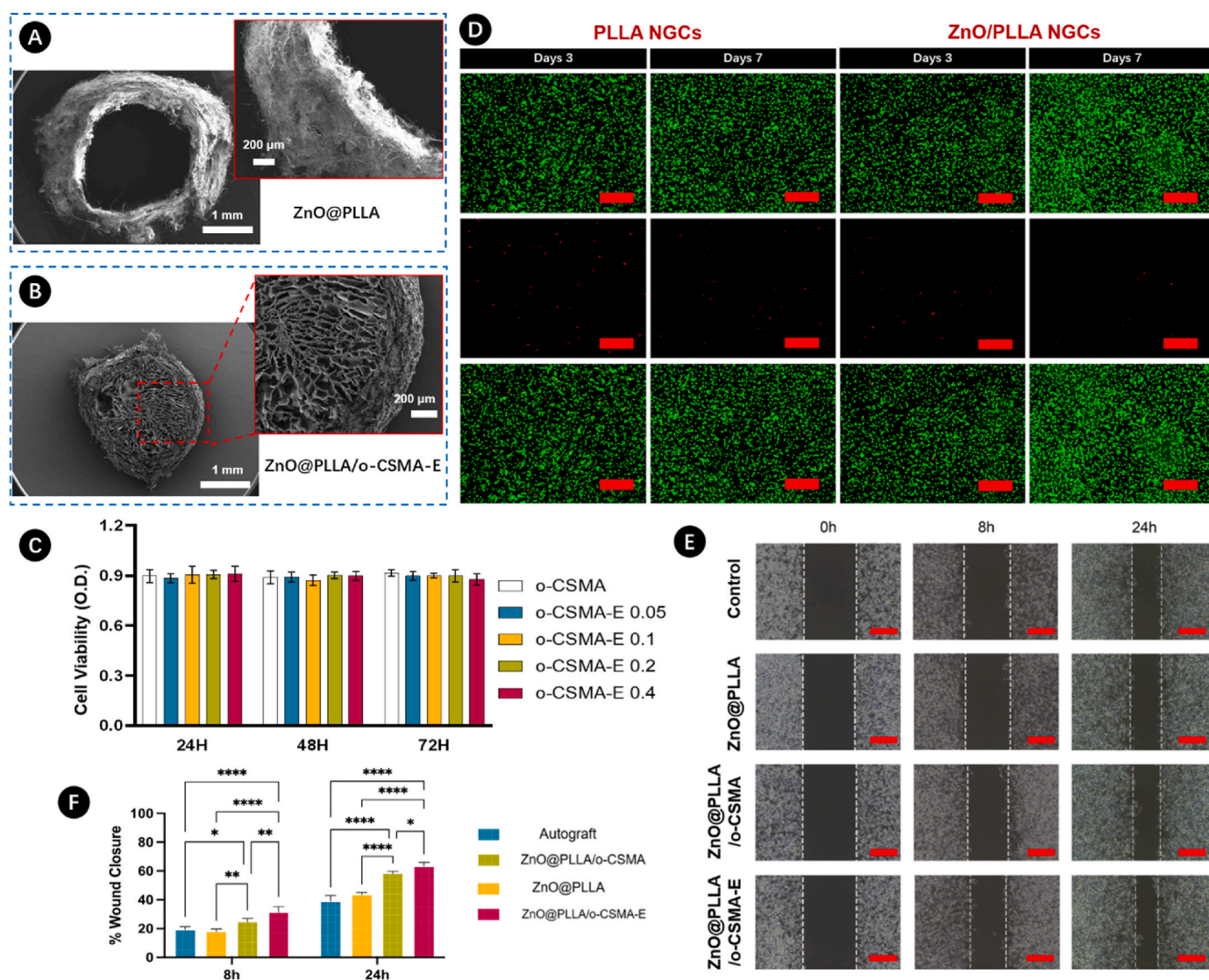

Fig. 6. Cross-sectional SEM images of A) ZnO@PLLA electrospinning NGCs; B) ZnO@PLLA NGCs loaded with O-CSMA-E hydrogel; C) Biocompatibility evaluation of PC12 cells cultured with NGCs made of PLLA and ZnO@PLLA with different ZnO content; D) Live/dead cell staining assay for PLLA and ZnO@PLLA NGCs, green indicates live cells, while red represents dead cells; E) PC12 cells scratch test analysis, the scratch area at the bare region at 0, 8, and 24 h (n = 3); F) Wound closure of PC12 cells quantitively analysis. The red scale bar indicates 100 μm. (For interpretation of the references to colour in this figure legend, the reader is referred to the Web version of this article.)

well-designed core structure may encourage Schwann cells to facilitate the repair of interrupted neural connections within the defined edges of the sheath. In this study, composite NGC was prepared using a nanofibrous ZnO@PLLA sheath (Fig. 6A) and o-CSMA-E core (Fig. 6B). This design was implemented to meet essential criteria such as graft stability, biocompatibility, controlled degradation, and fluid exchange. Moreover, cross-sectional SEM images of the NGC (Fig. 6A and **B**) show a well-defined outer sheath structure to facilitate active nourishment of cells growing in the conductive o-CSMA-E core part. A low level of cytotoxicity is one of the prerequisites for using the material in nerve repair [26]. In this regard, the impacts of NGCs loaded with different O-CSMA-E hydrogels on cell viability were assessed. To evaluate cell metabolic activity CCK-8 assay was performed on the scaffolds cultured for 24, 48, and 72 h (Fig. 6C). The results proved that NGS displays good biological activity, which can be mainly attributed to the high biological activity of dECM, promoting cell attachment and proliferation. Cell viability in all cases was above 85 %, with no statistically significant difference among the groups. Fluorescence staining was used to reassure NGC cytocompatibility (Fig. 6D). For this purpose, PC12 cells were cultured on the electrospinning PLLA and ZnO@PLLA constructs. Staining with Calcein/Propidium iodide (Calcein AM/PI) performed after 3 or 7 days allowed to distinguish live and dead cells. The images revealed nearly no dead cells, with more intense staining for cells cultured on ZnO@PLLA, proving that the materials were non-toxic to PC12 cells.

Cell migration, along with cell viability, is another crucial indicator of a material's ability to promote effective regeneration. To assess this, a scratch assay was conducted for cells cultured with ZnO@PLLA, ZnO@PLLA/o-CSMA, and ZnO@PLLA/o-CSMA-E, and the results were compared with the control (Fig. 6E). At the 8 h and 24 h intervals, observations indicated cellular migration towards the scratched area in all tested groups. Notably, a faster cell migration rate, as illustrated by wound closure in Fig. 6F, was observed in NGC samples incorporating both sheath and core components. It can be inferred that the presence of naturally derived dECM components positively influences PC12 cell migration. The *in vitro* tests suggest that engineered, composite NGCs may serve as a biomimetic platform enhancing cell survival and fostering cell migration, thus fulfilling essential elements for successful nerve regeneration.

3.5. NGCs performance for peripheral nerve regeneration in vivo

Peripheral nerves are responsible for transmitting electrical signals to the neuromuscular interfaces, contracting skeletal muscles, and enabling movement. Motility functions can be impaired in case of neural injuries; however, they can be restored if nerve connections are reestablished. Engineered NGCs can provide an efficient solution to navigate neural regeneration processes mimicking the structure and function of nerves along with a desirable environment. To evaluate the capability of composite NGCs to restore signal transmittance in injured nerves, a rat model with sciatic nerve defects was employed [61]. All surgical procedures were performed successfully without any complications (Fig. 7A). This study investigated the regenerative potential of ZnO@PLLA, ZnO@PLLA/o-CSMA, and ZnO@PLLA/o-CSMA-E and compared it with autograft, where the injured nerves were rotated 180° and implanted in the same place. At 4- and 8 weeks post-implantation, all NGCs remained intact, confirming their sufficient stability with the rat's gastrocnemius muscles 8 weeks post-surgery, presented in Fig. 7B.

One method for assessing peripheral nerve regeneration involves evaluating the weight and structure of the gastrocnemius muscle [62]. By comparing the wet weight ratio of the intact nerve with muscle and the weight of the NGC with muscle tissue (Fig. 7C), it becomes evident that weight restoration was most efficient in ZnO@PLLA/o-CSMA-E, which includes dECM along with the conductive hydrogel. Another approach to investigate the performance of regenerated nerves is through nerve electrophysiology testing and neural signal recording.

The percentages of Compound Muscle Action Potentials (CMAPs) amplitudes (Fig. 7D) for ZnO@PLLA/o-CSMA-E NGCs were not statistically different from the CMAP measured for the autograft. A similar trend was observed by Deng et al. in their chitosan double-layer conduit [26], demonstrating the high potency of chitosan-based materials on transmitted signal quality. Similarly, the motor nerve conduction velocities (Fig. 7E) measured for ZnO@PLLA/o-CSMA-E were close to those of their native counterparts. Overall, the ZnO@PLLA/o-CSMA-E conduits performed better in all 3 tests (Fig. 7C–E), than other grafts, demonstrating the relevance of material choice for the core and sheath part of the NGC. Furthermore, the gastrocnemius muscles were further treated using HE and Masson's staining (Fig. 7F). From HE and Masson's staining images, it was observed that the muscle fiber structure in ZnO@PLLA/o-CSMA-E group was clear and well-organized as that in the autograft group. According to the quantitative analysis, the percentage of muscle fiber area in ZnO@PLLA/o-CSMA-E group was higher than ZnO@PLLA/o-CSMA and ZnO@PLLA groups (Fig. 7G). However, the percentages of collagen fiber area in ZnO@PLLA/o-CSMA-E group displayed the lowest value compared to ZnO@PLLA/o-CSMA and ZnO@PLLA groups (Fig. 7H). In addition, there were no significant differences between ZnO@PLLA/o-CSMA-E group and the autograft group.

Sciatic Function Index (SFI) is a method used for peripheral nerve injury evaluation [63]. SFI for different groups was determined based on walking corridor analyses [64], as shown in Fig. 7I. SFI score was similar for autograft and ZnO@PLLA/o-CSMA-E conduit. The corresponding footprints in the autograft and Zn@PLLA/o-CSMA-E group were shorter and had distinguishable toes demonstrating a higher degree of motor function recovery compared toZnO@PLLA and ZnO@PLLA/o-CSMA group (Fig. 7K). The lowest score was assigned to pure ZnO@PLLA conduit, where footprints were longer, pointing to locomotive challenges. Data based on footprint analysis aligns with myelin basic protein (MBP) and neurofilament (NF) expression levels (Fig. 7J–L). Hampered expression of these factors may be due to the insufficient number of cells recruited for regeneration, which also translates to impaired locomotion restoration [65,66].

The microstructure of regenerated nerves after using ZnO@PLLA, ZnO@PLLA/o-CSMA, and ZnO@PLLA/o-CSMA-E conduits was observed by transmission electron microscopy (TEM) images (Fig. 8A). For TEM images, it could be apparently observed that ZnO@PLLA/o-CSMA-E conduit group displayed the thicker myelin sheaths than ZnO@PLLA and ZnO@PLLA/o-CSMA conduit groups, and morphology of the new formed myelin sheaths was very close to autograft group. In addition, according to the statistical analysis of myelin sheath thickness, G-ratio, and myelinated axon number (Fig. 8B–D), ZnO@PLLA and ZnO@PLLA/o-CSMA conduit groups exhibited significant differences compared to autograft group. However, the ZnO@PLLA/o-CSMA-E conduit group showed the highest myelin sheath thickness and myelinated axon number and the lowest G-ratio, confirming the effective myelination, optimal axonal function and integrity. Following HE and Masson staining, nerve regeneration was observed in all three conduit groups (Fig. 8E and **F**). Nerves in the ZnO@PLLA group appeared thin and non-uniform. In contrast, regenerated nerves in the ZnO@PLLA/o-CSMA-E group displayed a more consistently white appearance. Although disordered vessels and fibrous tissue were present in all conduit groups, the nerves in the ZnO@PLLA/o-CSMA-E conduit were less scattered and thicker. Notably, presence of collagen fibers was observed in the ZnO@PLLA and ZnO@PLLA/o-CSMA groups (Fig. 8F), indicating the formation of scar tissue [26]. Peripheral nerves are built from myelin sheaths and axons, with blood vessels and outer connective tissue. In our study, this characteristic core-sheath geometry was recapitulated by the outer area made of electrospinning fibers and the core part comprising dECM hydrogel. NGC in such a form could better support Schwann cell adhesion, proliferation, and graft colonization [56, 67], compared to other groups.

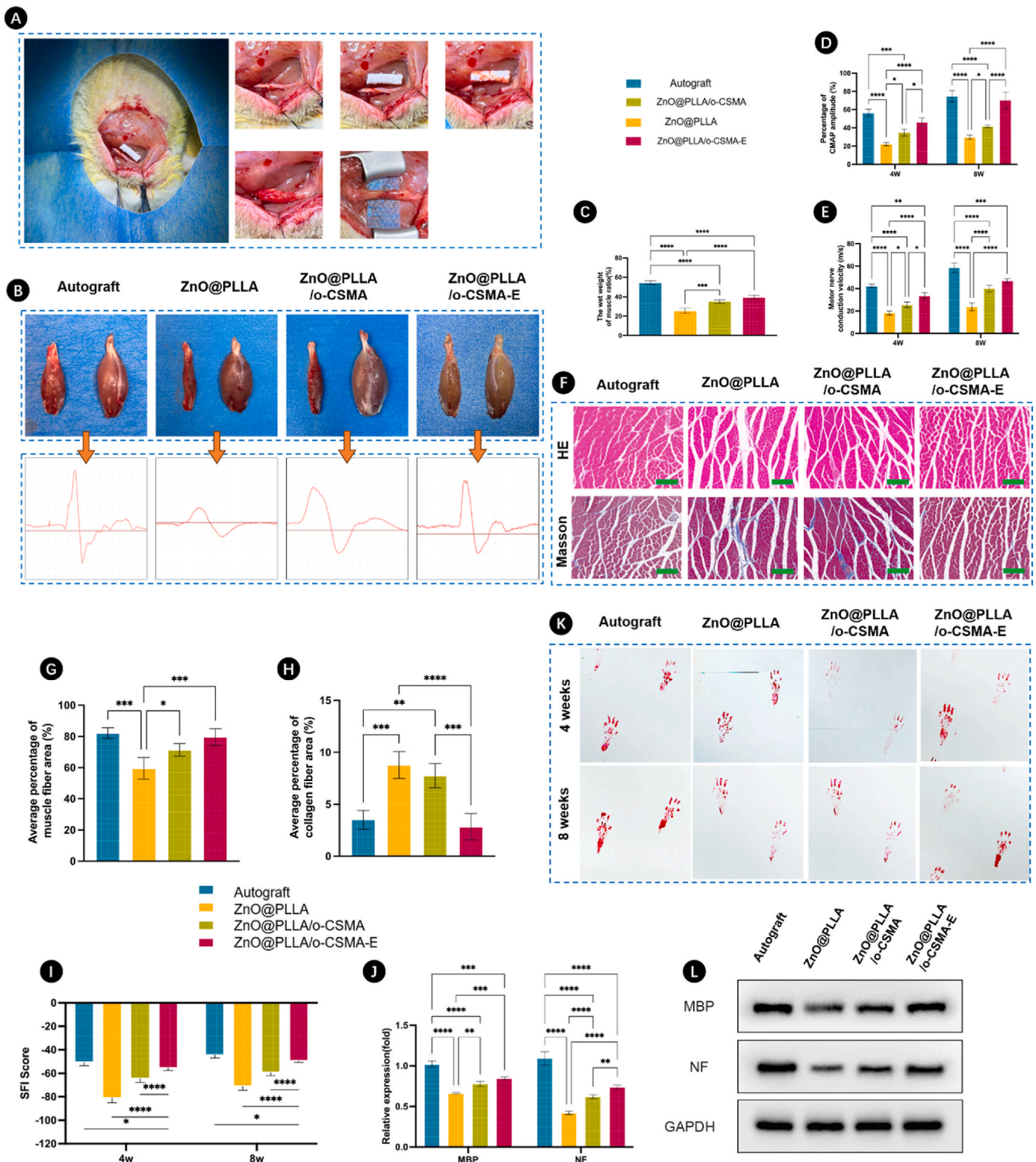In-depth immunofluorescence analysis (Fig. 9A–F) on rat sciatic

Fig. 7. A) Experimental procedure employed to investigate nerve regeneration in sciatic nerve defects; B) Representative images of gastrocnemius muscles in the four NGC groups with recorded electrical signals, the left side of each group represents the transplanted side, and the right side represents the physiological side; C) Wound closure post-operation; D) Ratio of the wet weight of the muscles for different groups; E) Percentages of (E) CMAP amplitude and (F) motor nerve conduction velocity for different groups after 4 and 8 weeks post-surgery. G) HE and Masson staining images of the gastrocnemius muscle on left side for each group after 8 weeks post-surgery, the green scale bars indicate 250 μm. H) Average percentage of muscle fiber area and I) average percentage of collagen area for each group calculated from HE and Masson staining images. J) Sciatic Function Index (SFI) assigned for different NGC groups; K) Levels of MBP and NF expression; L) Animal footprints used for analyzing abnormalities in locomotion after different times from surgery; M) Protein expression levels obtained from Western blots of proteins in regenerated sciatic nerve after 8 weeks with GAPDH used as a loading control antibody to normalize the levels of MBP and NF expression. Sample legend for Figures C, D, E, G, H, I, and J, statistical significance was determined using One-way ANOVA with Bonferroni's multiple comparison tests (*$p < 0.05$, **$p < 0.01$, ***$p < 0.001$, and ****$p < 0.0001$). (For interpretation of the references to colour in this figure legend, the reader is referred to the Web version of this article.)
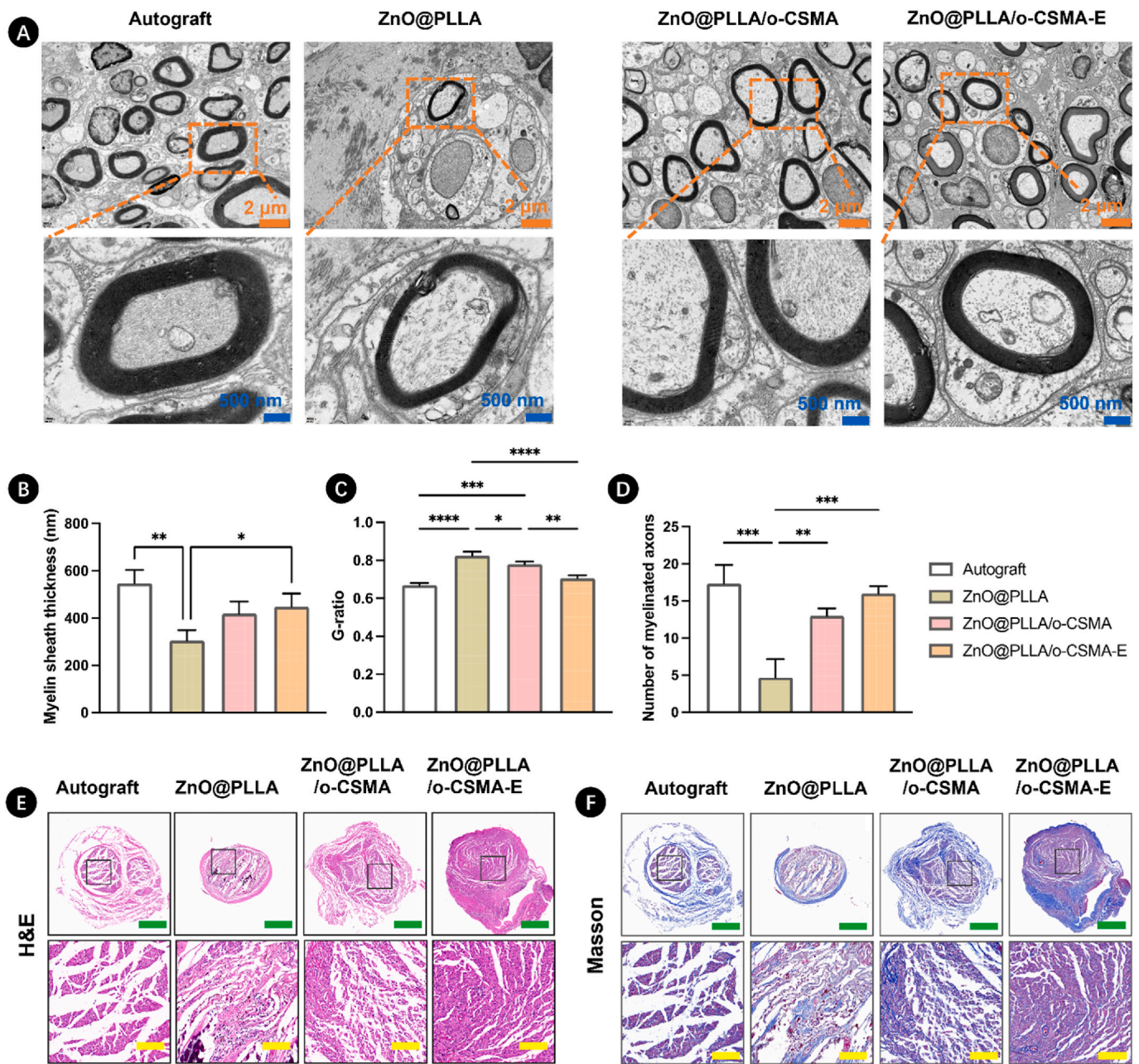
Fig. 8. A) Representative transmission electron microscopy (TEM) images of regenerated nerves. Statistical analysis of B) myelin sheath thickness, C) G-ratio in regenerated nerves, and D) the number of myelinated axons per 4 μm^2, $*p < 0.05$, $**p < 0.01$, $***p < 0.001$, and $****p < 0.0001$. Histological analysis of regenerated nerves in different NGC groups at 8 weeks post-surgery using (E) Hematoxylin and Eosin (HE), (F) Masson's trichrome staining, in H&E and Masson's staining, the green and yellow scale bars correspond to 500 μm and 100 μm, respectively. (For interpretation of the references to colour in this figure legend, the reader is referred to the Web version of this article.)

nerve samples 8 weeks post-surgery was employed to vigilantly evaluate the effect of our NGC on peripheral nerve regeneration. In the S100 staining, the ZnO@PLLA/o-CSMA-E demonstrated a high density of Schwann cells in the regenerative area. Notably, more mature axons, revealed in NF200 staining, dominate in the autograft group; however, they are noticeable in ZnO@PLLA sheaths in the presence of hydrogel filling as O-CSMA or O-CSMA-E. Staining based on MBP and ß Tubulin labelling showed further structural similarities in autograft and ZnO@PLLA/o-CSMA-E groups as myelinated axonal geometry was noticeable. The levels of MBP and NF200 protein expression align with the staining results for particular experimental groups (Fig. 9G–J).

4. Conclusions

Recognizing the intricate pathophysiology of nervous system injuries, the demand for the development of therapeutic approaches that address multiple facets of the repair and regeneration process over varied durations must be emphasized. In this regard, the utilization of electrospinning fiber sheaths, laden with bioactive hydrogel cores to emulate the native extracellular matrix in the nervous system was identified as a potential strategy for the introduction of favorable tunability characteristics that are necessary to evoke specific cell responses while simultaneously guiding regenerating neurons. The present study, therefore, engineered a novel nerve guidance conduit (NGC)
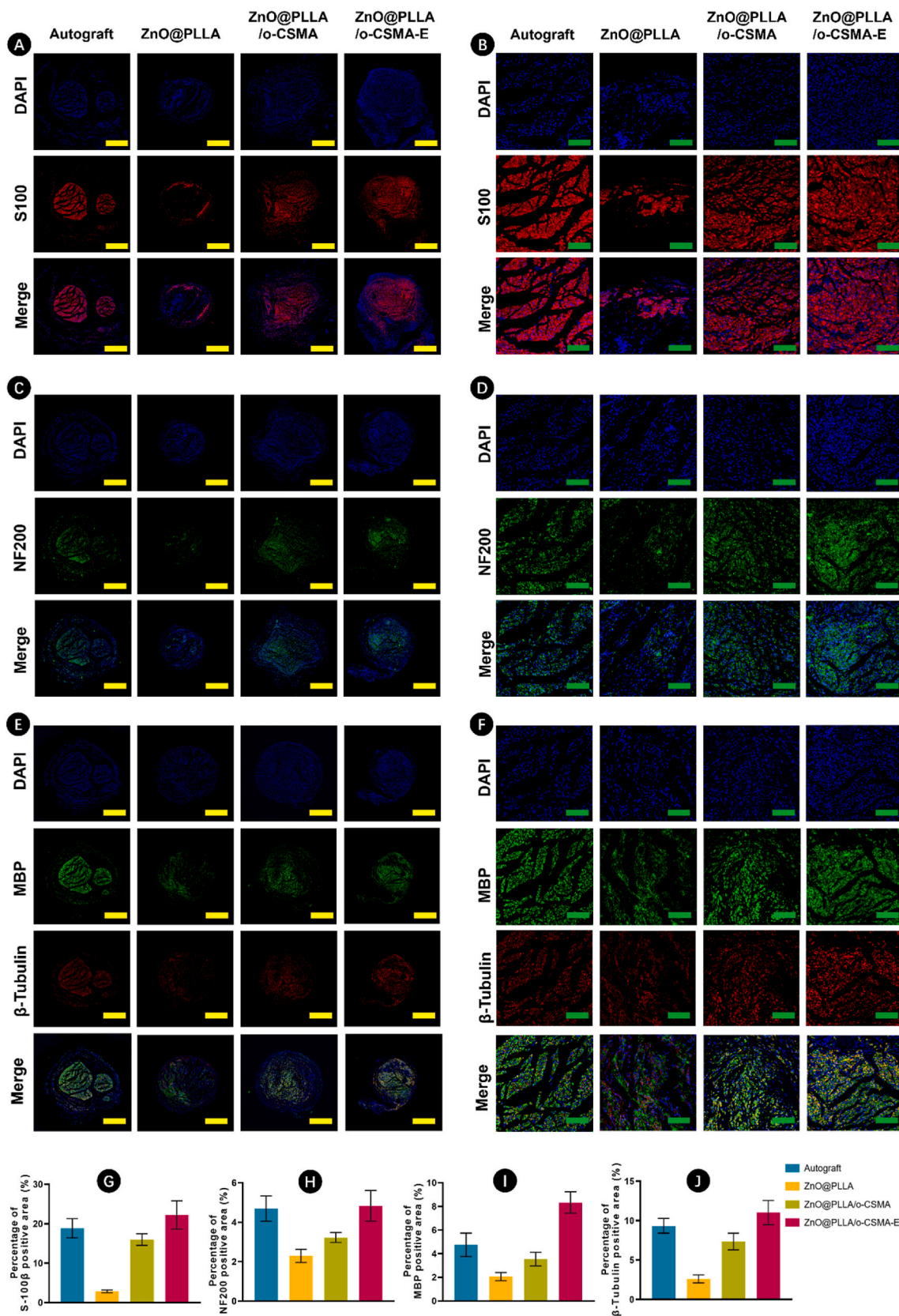
Fig. 9. Immunofluorescence staining of regenerated nerves at 8 weeks post-surgery. A-B) The DAPI (blue) stained cell nuclei in blue, A-B) S100 staining, C-D) NF200 staining, E-F) MBP and β-tubulin staining, which indicated the presence of Schwann cells and mature axons. The green and yellow scale bars correspond to 500 μm and 100 μm, respectively. Quantification of the positively stained areas for G) S-100 β; H) NF200; I) MBP; J) β-tubulin. (For interpretation of the references to colour in this figure legend, the reader is referred to the Web version of this article.)

that incorporated a dECM-based conductive hydrogel and subsequently demonstrated the potential of the NGC to establish a biomimetic microenvironment addressing diverse needs such as electrical stimulation, Schwann cell guidance, and consequently, accelerated axonal growth and myelination. The chitosan material selected as a composite material was able to confer antimicrobial properties. Further *In vivo* studies also revealed the comparability of the ZnO@PLLA/o-CSMA-E-mediated regeneration process to the processes guiding natural neural tissue restoration. When compared to traditional autografts, the ZnO@PLLA/o-CSMA-E NGCs demonstrated favorable performance in promoting nerve reconstruction and functional recovery, marking an advancement in NGC design and fabrication. While further research is necessary to optimize NGC design and explore its clinical applications in various scenarios of peripheral nerve damage, the obtained results underscore the potential of the developed biomimetic NGC as an effective alternative to autografts in treating peripheral nerve damage.

CRediT authorship contribution statement

Shuang Liu: Visualization, Methodology, Investigation, Formal analysis, Data curation. **Julia Simińska-Stanny:** Writing – original draft, Visualization. **Lizhao Yan:** Methodology, Investigation, Formal analysis. **Lihong Fan:** Writing – review & editing, Validation, Supervision, Resources, Project administration, Funding acquisition, Conceptualization. **Xiaoyue Ding:** Methodology, Investigation, Formal analysis, Data curation. **Tengda Ma:** Methodology, Investigation, Formal analysis, Data curation. **Wei Guo:** Methodology, Investigation, Formal analysis, Data curation. **Yingsong Zhao:** Methodology, Investigation, Formal analysis, Data curation. **Ming Li:** Methodology, Investigation, Formal analysis, Data curation. **Jianghai Chen:** Methodology, Investigation, Formal analysis, Data curation. **Oseweuba Valentine Okoro:** Writing – review & editing. **Armin Shavandi:** Writing – review & editing. **Lei Nie:** Writing – review & editing, Supervision, Resources, Project administration, Funding acquisition, Conceptualization.

Declaration of competing interest

The authors declare that they have no known competing financial interests or personal relationships that could have appeared to influence the work reported in this paper.

Acknowledgements

Appendix A. Supplementary data

Supplementary data to this article can be found online at https://doi.org/10.1016/j.mtbio.2024.101324.

Data availability

Data will be made available on request.

References

[1] E. Yu, Z. Chen, Y. Huang, Y. Wu, Z. Wang, F. Wang, M. Wu, K. Xu, W. Peng, A grooved conduit combined with decellularized tissues for peripheral nerve regeneration, J. Mater. Sci. Mater. Med. 34 (7) (2023) 35, https://doi.org/10.1007/s10856-023-06737-z.

[2] S. Behtaj, J.A.K. Ekberg, J.A. St John, Advances in electrospun nerve guidance conduits for engineering neural regeneration, Pharmaceutics 14 (2022) 219. https://doi.org/10.3390/pharmaceutics14020219.

[3] P. Zarrintaj, E. Zangene, S. Manouchehri, L.M. Amirabad, N. Baheiraei, M.R. Hadjighasem, M. Farokhi, M.R. Ganjali, B.W. Walker, M.R. Saeb, M. Mozafari, S. Thomas, N. Annabi, Conductive biomaterials as nerve conduits: recent advances and future challenges, Appl. Mater. Today 20 (2020) 100784, https://doi.org/10.1016/j.apmt.2020.100784.

[4] W. Zhou, M.S.U. Rahman, C. Sun, S. Li, N. Zhang, H. Chen, C.C. Han, S. Xu, Y. Liu, Perspectives on the novel multifunctional nerve guidance conduits: from specific regenerative procedures to motor function rebuilding, Adv. Mater. (2023) e2307805, https://doi.org/10.1002/adma.202307805.

[5] X. Zhang, Y. Ma, Z. Chen, H. Jiang, Z. Fan, Implantable nerve conduit made of a self-powered microneedle patch for sciatic nerve repair, Adv. Healthcare Mater. 12 (31) (2023) 2301729, https://doi.org/10.1002/adhm.202301729.

[6] P. Meena, A. Kakkar, M. Kumar, N. Khatri, R.K. Nagar, A. Singh, P. Malhotra, M. Shukla, S.K. Saraswat, S. Srivastava, R. Datt, S. Pandey, Advances and clinical challenges for translating nerve conduit technology from bench to bed side for peripheral nerve repair, Cell Tissue Res. 383 (2) (2021) 617–644, https://doi.org/10.1007/s00441-020-03301-x.

[7] Z. Wang, Y. Zheng, L. Qiao, Y. Ma, H. Zeng, J. Liang, Q. Ye, K. Shen, B. Liu, L. Sun, Z. Fan, 4D-Printed MXene-based artificial nerve guidance conduit for enhanced regeneration of peripheral nerve injuries, Adv. Healthcare Mater. 13 (23) (2024) 2401093, https://doi.org/10.1002/adhm.202401093.

[8] C. Hu, B. Liu, X. Huang, Z. Wang, K. Qin, L. Sun, Z. Fan, Sea cucumber-inspired microneedle nerve guidance conduit for synergistically inhibiting muscle atrophy and promoting nerve regeneration, ACS Nano 18 (22) (2024) 14427–14440, https://doi.org/10.1021/acsnano.4c00794.

[9] T. Wan, Y.-L. Wang, F.-S. Zhang, X.-M. Zhang, Y.-C. Zhang, H.-R. Jiang, M. Zhang, P.-X. Zhang, The porous structure of peripheral nerve guidance conduits: features, fabrication, and implications for peripheral nerve regeneration, Int. J. Mol. Sci. (2023).

[10] S. Gao, X. Chen, S. Lu, K. Meng, K.-Q. Zhang, H. Zhao, Recent advances on nerve guide conduits based on textile methods, Smart Materials in Medicine 4 (2023) 368–383, https://doi.org/10.1016/j.smaim.2022.12.001.

[11] A. Zennifer, M. Thangadurai, D. Sundaramurthi, S. Sethuraman, Additive manufacturing of peripheral nerve conduits – fabrication methods, design considerations and clinical challenges, SLAS Technology 28 (3) (2023) 102–126, https://doi.org/10.1016/j.slast.2023.03.006.

[12] J. Simińska-Stanny, F. Hachemi, G. Dodi, F.D. Cojocaru, I. Gardikiotis, D. Podstawczyk, C. Delporte, G. Jiang, L. Nie, A. Shavandi, Optimizing phenol-modified hyaluronic acid for designing shape-maintaining biofabricated hydrogel scaffolds in soft tissue engineering, Int. J. Biol. Macromol. (2023) 125201, https://doi.org/10.1016/j.ijbiomac.2023.125201.

[13] D. Podstawczyk, M. Nizioł, P. Śledzik, J. Simińska-Stanny, A. Dawiec-Liśniewska, A. Shavandi, Coaxial 4D printing of vein-inspired thermoresponsive channel hydrogel actuators, Adv. Funct. Mater. n/a(n/a) 2310514 https://doi.org/https://doi.org/10.1002/adfm.202310514.

[14] H. Javidi, A. Ramazani Saadatabadi, S.K. Sadrnezhaad, N. Najmoddin, Conductive nerve conduit with piezoelectric properties for enhanced PC12 differentiation, Sci. Rep. 13 (1) (2023) 12004, https://doi.org/10.1038/s41598-023-38456-4.

[15] M. Xu, Y. Wen, F. Niu, Q. Yang, C. Xiong, Z. Shi, Flexible piezoelectric generator based on PLLA/ZnO oriented fibers for wearable self-powered sensing, Compos. Appl. Sci. Manuf. 169 (2023) 107518, https://doi.org/10.1016/j.compositesa.2023.107518.

[16] R. Mao, B. Yu, J. Cui, Z. Wang, X. Huang, H. Yu, K. Lin, S.G.F. Shen, Piezoelectric stimulation from electrospun composite nanofibers for rapid peripheral nerve regeneration, Nano Energy 98 (2022) 107322, https://doi.org/10.1016/j.nanoen.2022.107322.

[17] F. Rao, Y. Wang, D. Zhang, C. Lu, Z. Cao, J. Sui, M. Wu, Y. Zhang, W. Pi, B. Wang, Y. Kou, X. Wang, P. Zhang, B. Jiang, Aligned chitosan nanofiber hydrogel grafted with peptides mimicking bioactive brain-derived neurotrophic factor and vascular endothelial growth factor repair long-distance sciatic nerve defects in rats, Theranostics 10 (4) (2020) 1590–1603, https://doi.org/10.7150/thno.36272.

[18] M.S. Namini, S. Ebrahimi-Barough, J. Ai, H.K. Jahromi, E. mikaeiliagah, M. Azami, N. Bahrami, N. Lotfibakhshaiesh, J. Saremi, S. Shirian, Tissue-engineered core–shell silk-fibroin/poly-l-lactic acid nerve guidance conduit containing encapsulated exosomes of human endometrial stem cells promotes peripheral nerve regeneration, ACS Biomater. Sci. Eng. 9 (6) (2023) 3496–3511, https://doi.org/10.1021/acsbiomaterials.3c00157.

[19] D.T. Wu, N. Jeffreys, M. Diba, D.J. Mooney, Viscoelastic biomaterials for tissue regeneration, Tissue Eng. C Methods 28 (7) (2022) 289–300, https://doi.org/10.1089/ten.tec.2022.0040.

[20] J. Kort-Mascort, S. Flores-Torres, O. Peza-Chavez, J.H. Jang, L.A. Pardo, S.D. Tran, J. Kinsella, Decellularized ECM hydrogels: prior use considerations, applications, and opportunities in tissue engineering and biofabrication, Biomater. Sci. 11 (2) (2023) 400–431, https://doi.org/10.1039/d2bm01273a.

[21] S. Liu, Y. Zhao, M. Li, L. Nie, Q. Wei, O.V. Okoro, H. Jafari, S. Wang, J. Deng, J. Chen, A. Shavandi, L. Fan, Bioactive wound dressing based on decellularized tendon and GelMA with incorporation of PDA-loaded asiaticoside nanoparticles for

scarless wound healing, Chem. Eng. J. 466 (2023) 143016, https://doi.org/10.1016/j.cej.2023.143016.

[22] Full-thickness skin wound healing using human placenta-derived extracellular matrix containing bioactive molecules, Tissue Eng. 19 (3–4) (2013) 329–339, https://doi.org/10.1089/ten.tea.2011.0738.

[23] C. Zheng, Z. Yang, S. Chen, F. Zhang, Z. Rao, C. Zhao, D. Quan, Y. Bai, J. Shen, Nanofibrous nerve guidance conduits decorated with decellularized matrix hydrogel facilitate peripheral nerve injury repair, Theranostics 11 (6) (2021) 2917–2931, https://doi.org/10.7150/thno.50825.

[24] F. Zhang, M. Zhang, S. Liu, C. Li, Z. Ding, T. Wan, P. Zhang, Application of hybrid electrically conductive hydrogels promotes peripheral nerve regeneration, Gels 8 (1) (2022), https://doi.org/10.3390/gels8010041.

[25] H. Xuan, S. Wu, Y. Jin, S. Wei, F. Xiong, Y. Xue, B. Li, Y. Yang, H. Yuan, A bioinspired self-healing conductive hydrogel promoting peripheral nerve regeneration, Adv. Sci. 10 (28) (2023) 2302519, https://doi.org/10.1002/advs.202302519.

[26] P. Deng, F. Chen, H. Zhang, Y. Chen, J. Zhou, Multifunctional double-layer composite hydrogel conduit based on chitosan for peripheral nerve repairing, Adv. Healthcare Mater. 11 (13) (2022) 2200115, https://doi.org/10.1002/adhm.202200115.

[27] M. Rahman, T. Mahady Dip, R. Padhye, S. Houshyar, Review on electrically conductive smart nerve guide conduit for peripheral nerve regeneration, J. Biomed. Mater. Res. 111 (12) (2023) 1916–1950, https://doi.org/10.1002/jbm.a.37595.

[28] L.a. Jiang, S. Tian, Y. Xie, X. Lv, S. Sun, High strength, conductivity, and bacteriostasis of the P(AM-co-AA)/Chitosan quaternary ammonium salt composite hydrogel through ionic crosslinking and hydrogen bonding, Langmuir 39 (25) (2023) 8698–8709, https://doi.org/10.1021/acs.langmuir.3c00646.

[29] F. Liu, X. Zhang, X. Xiao, Q. Duan, H. Bai, Y. Cao, Y. Zhang, M. Alee, L. Yu, Improved hydrophobicity, antibacterial and mechanical properties of polyvinyl alcohol/quaternary chitosan composite films for antibacterial packaging, Carbohydr. Polym. 312 (2023) 120755, https://doi.org/10.1016/j.carbpol.2023.120755.

[30] P. Liu, W. Meng, S. Wang, Y. Sun, M.A. Ashraf, Quaternary ammonium salt of chitosan: preparation and antimicrobial property for paper, Open Med. 10 (1) (2015) 473–478, https://doi.org/10.1515/med-2015-0081.

[31] C. Intini, L. Elviri, J. Cabral, S. Mros, C. Bergonzi, A. Bianchera, L. Flammini, P. Govoni, E. Barocelli, R. Bettini, M. McConnell, 3D-printed chitosan-based scaffolds: an in vitro study of human skin cell growth and an in-vivo wound healing evaluation in experimental diabetes in rats, Carbohydr. Polym. 199 (2018) 593–602, https://doi.org/10.1016/j.carbpol.2018.07.057.

[32] X. Yang, L. Huang, X. Yi, S. Huang, B. Duan, A. Yu, Multifunctional chitin-based hollow nerve conduit for peripheral nerve regeneration and neuroma inhibition, Carbohydr. Polym. 289 (2022) 119443, https://doi.org/10.1016/j.carbpol.2022.119443.

[33] M. Zhang, H. An, F. Zhang, H. Jiang, T. Wan, Y. Wen, N. Han, P. Zhang, Prospects of using chitosan-based biopolymers in the treatment of peripheral nerve injuries, Int. J. Mol. Sci. 24 (16) (2023) 12956.

[34] D.A. Taylor, L.C. Sampaio, Z. Ferdous, A.S. Gobin, L.J. Taite, Decellularized matrices in regenerative medicine, Acta Biomater. 74 (2018) 74–89, https://doi.org/10.1016/j.actbio.2018.04.044.

[35] A.u.R. Khan, K. Huang, Z. Khalaji, T. Zhu, Y. Morsi, A. Aldalbahi, M. El-Newehy, X. Yan, X. Mo, Exploration of the antibacterial and wound healing potential of a PLGA/silk fibroin based electrospun membrane loaded with zinc oxide nanoparticles, J. Mater. Chem. B 9 (5) (2021) 1452–1465, https://doi.org/10.1039/D0TB02822C.

[36] J. Cao, G. He, X. Ning, X. Chen, L. Fan, M. Yang, Y. Yin, W. Cai, Preparation and properties of O-chitosan quaternary ammonium salt/polyvinyl alcohol/graphene oxide dual self-healing hydrogel, Carbohydr. Polym. 287 (2022), https://doi.org/10.1016/j.carbpol.2022.119318.

[37] W. Guo, X. Gao, X. Ding, P. Ding, Y. Han, Q. Guo, Y. Ma, O.V. Okoro, Y. Sun, G. Jiang, Self-adhesive and self-healing hydrogel dressings based on quaternary ammonium chitosan and host-guest interacted silk fibroin, Colloids Surf. A Physicochem. Eng. Asp. (2024) 133145.

[38] L. Nie, M. Hou, T. Wang, M. Sun, R. Hou, Nanostructured selenium-doped biphasic calcium phosphate with in situ incorporation of silver for antibacterial applications, Sci. Rep. 10 (1) (2020) 13738.

[39] L. Yan, S. Liu, J. Wang, X. Ding, Y. Zhao, N. Gao, Z. Xia, M. Li, Q. Wei, O.V. Okoro, Y. Sun, L. Nie, A. Shavandi, G. Jiang, J. Chen, L. Fan, Y. Weng, Constructing nerve guidance conduit using dECM-doped conductive hydrogel to promote peripheral nerve regeneration, Adv. Funct. Mater. 34 (38) (2024) 2402698, https://doi.org/10.1002/adfm.202402698.

[40] E. Elnabawy, A.H. Hassanain, N. Shehata, A. Popelka, R. Nair, S. Yousef, I. Kandas, Piezoelastic PVDF/TPU nanofibrous composite membrane: fabrication and characterization, Polymers 11 (10) (2019) 1634.

[41] L. Nie, Q. Wei, M. Sun, P. Ding, L. Wang, Y. Sun, X. Ding, O.V. Okoro, G. Jiang, A. Shavandi, Injectable, self-healing, transparent, and antibacterial hydrogels based on chitosan and dextran for wound dressings, Int. J. Biol. Macromol. 233 (2023) 123494, https://doi.org/10.1016/j.ijbiomac.2023.123494.

[42] W. Chang, M.B. Shah, G. Zhou, K. Walsh, S. Rudraiah, S.G. Kumbar, X. Yu, Polymeric nanofibrous nerve conduits coupled with laminin for peripheral nerve regeneration, Biomed. Mater. 15 (3) (2020) 035003, https://doi.org/10.1088/1748-605X/ab6994.

[43] S. Liu, Y. Zhao, M. Li, L. Nie, Q. Wei, O.V. Okoro, H. Jafari, S. Wang, J. Deng, J. Chen, Bioactive wound dressing based on decellularized tendon and GelMA with incorporation of PDA-loaded asiaticoside nanoparticles for scarless wound healing, Chem. Eng. J. 466 (2023) 143016.

[44] C.-Y. Yang, W.-Y. Huang, L.-H. Chen, N.-W. Liang, H.-C. Wang, J. Lu, X. Wang, T.-W. Wang, Neural tissue engineering: the influence of scaffold surface topography and extracellular matrix microenvironment, J. Mater. Chem. B 9 (3) (2021) 567–584, https://doi.org/10.1039/D0TB01605E.

[45] S. Zhao, W.-C. Tsen, C. Gong, 3D nanoflower-like layered double hydroxide modified quaternized chitosan/polyvinyl alcohol composite anion conductive membranes for fuel cells, Carbohydr. Polym. 256 (2021) 117439, https://doi.org/10.1016/j.carbpol.2020.117439.

[46] C.H. Kim, J.W. Choi, H.J. Chun, K.S. Choi, Synthesis of chitosan derivatives with quaternary ammonium salt and their antibacterial activity, Polym. Bull. 38 (4) (1997) 387–393, https://doi.org/10.1007/s002890050064.

[47] M. He, C.-C. Chu, Dual stimuli responsive glycidyl methacrylate chitosan-quaternary ammonium hybrid hydrogel and its bovine serum albumin release, J. Appl. Polym. Sci. 130 (5) (2013) 3736–3745, https://doi.org/10.1002/app.39635.

[48] X. Lin, J. Liu, F. Zhou, Y. Ou, J. Rong, J. Zhao, Poly(2-hydroxyethyl methacrylate-co-quaternary ammonium salt chitosan) hydrogel: a potential contact lens material with tear protein deposition resistance and antimicrobial activity, Biomater. Adv. 136 (2022) 212787, https://doi.org/10.1016/j.bioadv.2022.212787.

[49] L. Zhu, K.M. Bratlie, pH sensitive methacrylated chitosan hydrogels with tunable physical and chemical properties, Biochem. Eng. J. 132 (2018) 38–46, https://doi.org/10.1016/j.bej.2017.12.012.

[50] M. Yan, X. An, Z. Jiang, S. Duan, A. Wang, X. Zhao, Y. Li, Effects of cross-linking with EDC/NHS and genipin on characterizations of self-assembled fibrillar gel prepared from tilapia collagen and alginate, Polym. Degrad. Stabil. 200 (2022) 109929, https://doi.org/10.1016/j.polymdegradstab.2022.109929.

[51] M.Y. Jin, T.E. Weaver, A. Farris, M. Gupta, A. Abd-Elsayed, Neuromodulation for peripheral nerve regeneration: systematic review of mechanisms and in vivo highlights, Biomedicines (2023), https://doi.org/10.3390/biomedicines11041145.

[52] X. Mao, T. Li, J. Cheng, M. Tao, Z. Li, Y. Ma, R. Javed, J. Bao, F. Liang, W. Guo, X. Tian, J. Fan, T. Yu, Q. Ao, Nerve ECM and PLA-PCL based electrospun bilayer nerve conduit for nerve regeneration, Front. Bioeng. Biotechnol. (2023), https://doi.org/10.3389/fbioe.2023.1103435.

[53] J. Beal, N.G. Farny, T. Haddock-Angelli, et al., Robust estimation of bacterial cell count from optical density, Commun Biol 3 (2020) 512. https://doi.org/10.1038/s42003-020-01127-5.

[54] M. Asadian, K.V. Chan, M. Norouzi, S. Grande, P. Cools, R. Morent, N. De Geyter, Fabrication and plasma modification of nanofibrous tissue engineering scaffolds, Nanomaterials (2020).

[55] M. Rahmati, D.K. Mills, A.M. Urbanska, M.R. Saeb, J.R. Venugopal, S. Ramakrishna, M. Mozafari, Electrospinning for tissue engineering applications, Prog. Mater. Sci. 117 (2021) 100721, https://doi.org/10.1016/j.pmatsci.2020.100721.

[56] D.L. Puhl, J.L. Funnell, D.W. Nelson, M.K. Gottipati, R.J. Gilbert, Electrospun fiber scaffolds for engineering glial cell behavior to promote neural regeneration, Bioengineering (2021).

[57] C.R. Mendes, G. Dilarri, C.F. Forsan, V.d.M.R. Sapata, P.R.M. Lopes, P.B. de Moraes, R.N. Montagnolli, H. Ferreira, E.D. Bidoia, Antibacterial action and target mechanisms of zinc oxide nanoparticles against bacterial pathogens, Sci. Rep. 12 (1) (2022) 2658, https://doi.org/10.1038/s41598-022-06657-y.

[58] J. Pasquet, Y. Chevalier, J. Pelletier, E. Couval, D. Bouvier, M.-A. Bolzinger, The contribution of zinc ions to the antimicrobial activity of zinc oxide, Colloids Surf. A Physicochem. Eng. Asp. 457 (2014) 263–274, https://doi.org/10.1016/j.colsurfa.2014.05.057.

[59] M.F.B. Daud, K.C. Pawar, F. Claeyssens, A.J. Ryan, J.W. Haycock, An aligned 3D neuronal-glial co-culture model for peripheral nerve studies, Biomaterials 33 (25) (2012) 5901–5913, https://doi.org/10.1016/j.biomaterials.2012.05.008.

[60] F. Pragati, S. Gangopadhyay, S. Pande, Synthesis of ZnO/Au and ZnO/Ag nano-particles and their photocatalytic application using UV and visible light, RSC Adv. 4 (2014) 294962, https://doi.org/10.1039/c4ra03158j.

[61] Q. Siwei, N. Ma, W. Wang, S. Chen, Q. Wu, Y. Li, Z. Yang, Construction and effect evaluation of different sciatic nerve injury models in rats 13 (1) (2022) 38–51, https://doi.org/10.1515/tnsci-2022-0214.

[62] P.B. Jaiswal, A.W. English, Chemogenetic enhancement of functional recovery after a sciatic nerve injury, European Journal of Neroscience (2017), https://doi.org/10.1111/ejn.13550.

[63] P. Dinh, A. Hazel, W. Palispis, S. Suryadevara, R. Gupta, Functional assessment after sciatic nerve injury in a rat model, Microsurgery 29 (8) (2009) 644–649, https://doi.org/10.1002/micr.20685.

[64] T. Kaplan, I. Kafa, M. Cansev, A. Bekar, N. Karli, M. Taşkapılıoğlu, F. Kanar, Investigation of the dose-dependency of citicoline effects on nerve regeneration and functional recovery in a rat model of sciatic nerve injury, Turkish neurosurgery 24 (2014) 54–62, https://doi.org/10.5137/1019-5149.JTN.8451-13.0.

[65] L. Liu, D. Tian, C. Liu, K. Yu, J. Bai, Metformin enhances functional recovery of peripheral nerve in rats with sciatic nerve crush injury, Med. Sci. Mon. Int. Med. J. Exp. Clin. Res. 25 (2019) 10067–10076, https://doi.org/10.12659/MSM.918277.

[66] S. Chen, Z. Du, J. Zou, S. Qiu, Z. Rao, S. Liu, X. Sun, Y. Xu, Q. Zhu, X. Liu, H.-Q. Mao, Y. Bai, D. Quan, Promoting neurite growth and Schwann cell migration by the harnessing decellularized nerve matrix onto nanofibrous guidance, ACS Appl. Mater. Interfaces 11 (19) (2019) 17167–17176, https://doi.org/10.1021/acsami.9b01066.

[67] D. Li, X. Pan, B. Sun, T. Wu, W. Chen, C. Huang, Q. Ke, H.A. Ei-Hamshary, S.S. Al-Deyab, X. Mo, Nerve conduits constructed by electrospun P(LLA-CL) nanofibers

and PLLA nanofiber yarns, J. Mater. Chem. B 3 (45) (2015) 8823–8831, https://doi.org/10.1039/C5TB01402F.